Redox Biology 73 (2024) 103207

Contents lists available at ScienceDirect

Redox Biology

journal homepage: www.elsevier.com/locate/redox

Redistribution of defective mitochondria-mediated dihydroorotate dehydrogenase imparts 5-fluorouracil resistance in colorectal cancer

Shuohui Dong [a,1], Mingguang Zhang [b,1], Zhiqiang Cheng [a], Xiang Zhang [a], Weili Liang [a], Songhan Li [c], Linchuan Li [d], Qian Xu [d], Siyi Song [d], Zitian Liu [a], Guangwei Yang [a], Xiang Zhao [a], Ze Tao [a], Shuo Liang [e,**], Kexin Wang [a,***], Guangyong Zhang [d,****], Sanyuan Hu [a,*]

[a] Department of General Surgery, Qilu Hospital of Shandong University, No. 107 Wenhua Xilu, Jinan, Shandong, 250012, China
[b] Department of Colorectal Surgery, National Cancer Center/National Clinical Research Center for Cancer/Cancer Hospital, Chinese Academy of Medical Sciences and Peking Union Medical College, Beijing, 100021, China
[c] Department of General Surgery, Peking University People's Hospital, Beijing, 100044, China
[d] Department of General Surgery, Shandong Provincial Qianfoshan Hospital, The First Hospital Affiliated with Shandong First Medical University, Jinan, Shandong, 250014, China
[e] Department of Otolaryngology-Head and Neck Surgery, Shandong Provincial ENT Hospital, Cheeloo College of Medicine, Shandong University, No. 4, Duanxing West Road, Jinan, Shandong,250022, China

ARTICLE INFO

Keywords:
Colorectal cancer
Chemoresistance
Lipid metabolic reprogramming
Ferroptosis
Dihydroorotate dehydrogenase

ABSTRACT

Although 5-fluorouracil (5-FU) is the primary chemotherapy treatment for colorectal cancer (CRC), its efficacy is limited by drug resistance. Ferroptosis activation is a promising treatment for 5-FU-resistant cancer cells; however, potential therapeutic targets remain elusive. This study investigated ferroptosis vulnerability and dihydroorotate dehydrogenase (DHODH) activity using stable, 5-FU-resistant CRC cell lines and xenograft models. Ferroptosis was characterized by measuring malondialdehyde levels, assessing lipid metabolism and peroxidation, and using mitochondrial imaging and assays. DHODH function is investigated through gene knockdown experiments, tumor behavior assays, mitochondrial import reactions, intramitochondrial localization, enzymatic activity analyses, and metabolomics assessments. Intracellular lipid accumulation and mitochondrial DHODH deficiency led to lipid peroxidation overload, weakening the defense system of 5-FU-resistant CRC cells against ferroptosis. DHODH, primarily located within the inner mitochondrial membrane, played a crucial role in driving intracellular pyrimidine biosynthesis and was redistributed to the cytosol in 5-FU-resistant CRC cells. Cytosolic DHODH, like its mitochondrial counterpart, exhibited dihydroorotate catalytic activity and participated in pyrimidine biosynthesis. This amplified intracellular pyrimidine pools, thereby impeding the efficacy of 5-FU treatment through molecular competition. These findings contribute to the understanding of 5-FU resistance mechanisms and suggest that ferroptosis and DHODH are promising therapeutic targets for patients with CRC exhibiting resistance to 5-FU.

1. Introduction

Colorectal cancer (CRC) is a global malignancy [1]. The primary CRC chemotherapy agent is 5-fluorouracil (5-FU) [2,3], which suppresses tumor growth by inhibiting thymidylate synthetase-mediated pyrimidine synthesis. Despite its widespread use in the treatment of advanced or metastatic CRC, the efficacy of 5-FU is limited by drug resistance in most treated patients [4]. Hence, gaining a comprehensive understanding of the mechanisms behind 5-FU resistance in CRC and exploring potential treatment combinations to enhance its effectiveness and that of other fluorouracil analogs are crucial.

* Corresponding author.
** Corresponding author.
*** Corresponding author.
**** Corresponding author.
E-mail addresses: shuoliang_sdent@163.com (S. Liang), wkx3726@163.com (K. Wang), guangyongzhang@hotmail.com (G. Zhang), drsanyuanhu@163.com (S. Hu).
[1] S.D. and M.Z. contributed equally to this work.

https://doi.org/10.1016/j.redox.2024.103207
Received 8 May 2024; Accepted 22 May 2024
Available online 23 May 2024

Abbreviations

5-FU	5-fluorouracil
ALA	alpha-linolenic acid
ARA	arachidonic acid
BAP1	BRCA1-associated protein 1
BH4	tetrahydrobiopterin
CAD	carbamoyl phosphate synthetase 2-aspartate carbamoyltransferase-dihydroorotase
CDX	cell line-derived xenograft
CoQH2	ubiquinol
CRC	Colorectal cancer
DHA	docosahexaenoic acid
DHO	dihydroorotate
DHODH	dihydroorotate dehydrogenase
DPA	docosapentaenoic acid
dTMP	deoxythymidine monophosphate
dUMP	deoxyuridine monophosphate
EPA	eicosapentaenoic acid
FABP1	fatty acid binding protein 1
FAO	fatty acid oxidation
FASN	fatty acid synthase
FATP4	fatty acid transport protein 4
FSP1	ferroptosis suppressor protein 1
GCH1	GTP cyclohydrolase 1
$GPX4^{Cyto}$	GPX4 in the cytosol
$GPX4^{Mito}$	GPX4 in the mitochondria
LA	linoleic acid
LDs	lipid droplets
LPO	lipid peroxidation
MUFAs	monounsaturated fatty acids
n-3	omega-3
n-6	omega-6
OA	oleic acid
OCR	oxygen-consumption rate
PA	palmitic acid
PDX	patient-derived xenograft
PUFAs	polyunsaturated fatty acids
ROS	reactive oxygen species
RPMI-1640	Roswell Park Memorial Institute 1640 medium
SD	standard deviation
SFAs	saturated fatty acids
SLC7A11	solute carrier family 7 member 11
SPF	specific-pathogen-free
TS	thymidylate synthase
UMP	uridine monophosphate

Recent research, including our work, highlights lipid metabolic reprogramming as a defining trait of cancer that enables cancer cells to evade chemotherapy [5–7]. Numerous studies have addressed metabolic reprogramming as a significant characteristic of chemoresistance, and interventions targeting metabolic abnormalities have emerged as viable therapeutic options [8–11]. However, the precise attributes of lipid metabolic reprogramming following 5-FU treatment in CRC remain largely unknown.

Ferroptosis, an iron-dependent cell death pathway [12], has demonstrated promise in therapy-refractory cancer cells in specific states, such as chemoresistant cells [13–15]. Although it has been identified that lipid peroxide overload triggers ferroptosis [16], the understanding of lipid metabolic reprogramming to ferroptotic vulnerability in chemoresistance is limited. Additionally, another essential element in ferroptosis is the defense mechanism [17]. Recent research indicates that mitochondria may house additional ferroptosis defense systems [18]. Our previous study detected an association between the presence of aberrant mitochondria and 5-FU resistance in CRC [19]. Therefore, investigating whether this phenomenon is linked to ferroptosis susceptibility may be valuable.

Dihydroorotate dehydrogenase (DHODH)-ubiquinol (CoQH2) is a newly discovered ferroptosis defense system in mitochondria [18]. DHODH inhibitors can induce ferroptosis and impact cancer therapy [20]. Importantly, DHODH is an essential enzyme for pyrimidine biosynthesis and cell proliferation [21], indicating that DHODH inhibition could be a potential cancer treatment strategy [22,23]. Considering that 5-FU is an analog of uracil and its activity is closely linked to pyrimidine metabolism, we explored the diverse functions of DHODH in regulating CRC cell responses to 5-FU chemotherapy.

Mechanistically, we report that intracellular lipid accumulation results in lipid peroxidation (LPO) overload, whereas mitochondrial DHODH deficiency weakens the ferroptosis defense system. The combination of these factors makes 5-FU-resistant CRC cells susceptible to ferroptosis. Moreover, mitochondrial DHODH redistribution to the cytosol increases intracellular pyrimidine pools, thereby impeding the effectiveness of 5-FU through molecular competition. Clinically, targeting ferroptosis or DHODH presents novel therapeutic prospects for treating patients with CRC exhibiting resistance to 5-FU therapies.

2. Material and methods

2.1. Chemicals

In this study, cells and mice were treated with additional supplemental fatty acids (all from Sigma-Aldrich) including as palmitic acid (PA), oleic acid (OA), linoleic acid (LA), arachidonic acid (ARA), docosapentaenoic acid (DPA), alpha-linolenic acid (ALA), eicosapentaenoic acid (EPA), and docosahexaenoic acid (DHA); fatty acid oxidation (FAO) inhibitor etomoxir; trifluorocarbonylcyanide phenylhydrazone (FCCP); chemotherapeutic agents including 5-FU (Abcam), irinotecan (MedChemExpress), and oxaliplatin (MedChemExpress); apoptosis inducer etoposide (Selleck); necroptosis inhibitor necrostatin-1 (MedChemExpress); ferroptosis inhibitors including ferrostatin-1 (MedChemExpress) and liproxstatin-1 (MedChemExpress); ferroptosis inducers including RSL3 (Selleck) and erastin (MedChemExpress); myristoylation inhibitor IMP-1088 (MedChemExpress); ATP production inhibitors including oligomycin (MedChemExpress) and carboxyatractyloside (MedChemExpress); and DHODH inhibitors including brequinar (Selleck) and teriflunomide (Selleck).

2.2. Cell lines

HCT8, HCT15, HCT116, LoVo, SW480, HT-29, Caco-2, and T84 CRC cell lines were obtained from KeyGEN Biotech and Cyagen Biosciences. Cell line identities were confirmed by short tandem repeat profiling, and all cell lines were positive for Mycoplasma (tested using a mycoplasma PCR detection kit from Sigma-Aldrich).

For 2D culture, cells were cultured in Roswell Park Memorial Institute 1640 medium (RPMI-1640) supplemented with 10 % (v/v) fetal bovine serum (FBS) and 1 % (v/v) penicillin/streptomycin at 37 °C with a humidified atmosphere and 5 % CO_2. Cells were passaged using 0.25 % trypsin-EDTA digestion. Cells were cultured in 10 cm plates and then transferred into 6-, 24-, or 96-well plates, or 15 cm plates depending on the experiment.

For 3D culture, 1000 cells were seeded in 96-well ultra-low attachment spheroid microplates (Corning). Treatment was initiated three days after cell seeding, and the culture and treatment system were replaced every three days. The 3D spheroids were monitored using an

Axio Vert.A1 inverted phase-contrast microscope (Zeiss), and the longest diameter of the spheroids was measured to calculate the spherical volume.

2.3. Patient-derived organoids (PDO)

The tissue dissociation medium (AIMINGMED) was utilized to rinse the tissue in a 10 cm Petri dish, followed by the use of scissors to section surgical specimens into small fragments, which were then transferred to a 15 mL conical tube. Subsequently, additional tissue dissociation medium was added to the conical tube, and the mixture was incubated at 37 °C with agitation. The progression of the digestion process was carefully monitored under a microscope, and the digestion was halted once the majority of cell clusters reached a diameter of less than 200 μm. D-PBS was then added to the conical tube to resuspend the pellet, and the mixture was filtered using a 100 μm cell strainer. The filtered cells were collected and centrifuged at 300 g for 5 min. The Matrigel (Corning) containing cells were plated in 50 μL droplets at the center of each well of a 24-well cell culture plate. The plate was then covered with a lid and placed in a cell culture incubator for 5 min. Subsequently, the plate was inverted in the incubator for 25 min to promote the formation of domes. Following dome formation, 600 μL of 37 °C organoid complete medium (AIMINGMED) was carefully added to each well without disturbing the domes. The culture plate was covered with a lid and subsequently incubated in a cell culture incubator set at 37 °C and 5 % CO_2. A complete medium change was conducted every 2–3 days by removing the existing medium and replacing it with fresh complete medium at room temperature.

2.4. In vivo mouse studies

Five mice were group-housed per cage under specific-pathogen-free (SPF) conditions. Feeding conditions were maintained at 25 ± 1 °C with a relative humidity of 50%–70 %, and the mice were maintained under a 12 h light/12 h dark cycle. The mice were provided filtered tap water and a standard rodent diet (NIH-41 irradiated diet). Alternatively, an OA-rich diet (supplemented with 100 g of olive oil per kg) and a DHA-rich diet (supplemented with 100 g of MorDHA oil per kg) were provided to the polyunsaturated fatty acid (PUFA)-treated groups. The three experimental diets were formulated to be isocaloric (3980 kcal kg^{-1}). The mice were sacrificed when the tumor dimensions reached 15 mm. None of the mice exhibited infections, wounds, or an obvious loss of body weight in the present study. The tumor volume was measured every three days until the endpoint and calculated using Equation (1).

$$\text{Volume} = \text{Length} \times \text{Width}^2 \times 0.52 \quad (1)$$

For cell line-derived xenograft (CDX) models, 4-week-old male athymic BALB/c nude mice were purchased from SPF Biotechnology Company, Ltd. (Beijing, China). Adaptive feeding with a standard, OA-rich, or DHA-rich diet was administered for 2 weeks, and the 6-week-old mice were then used as CDX models. Cancer cells were harvested in the logarithmic phase and suspended in cold phosphate-buffered saline. The cells (5×10^6) were injected subcutaneously into the underarm of the right forelimb. The cancer cells were allowed to proliferate for 1 week until measurable tumors were present. Different groups of mice were injected with 5-FU (25 mg kg^{-1}, three times a week, intraperitoneally), RSL3 (100 mg kg^{-1}, twice weekly, intratumorally), or saline (as a negative control).

For patient-derived xenograft (PDX) models, 4-week-old male NOG mice were purchased from Weitong Lihua Experimental Animal Technology Company, Ltd. (Beijing). Adaptive feeding with a standard, OA-rich, or DHA-rich diet was administered for 2 weeks, and the 6-week-old mice were then used as PDX models. PDX tumor specimens were obtained from a male patient with rectal cancer (TNM stage III) at the Qilu Hospital of Shandong University who had received neoadjuvant chemotherapy containing 5-FU and subsequent surgery. Fresh tumor tissues (third passage) were trimmed and cut into 1–2 mm blocks. The tissues were placed in RPMI-1640 medium supplemented with 50 % (v/v) FBS and 1 % (v/v) penicillin/streptomycin and stored on ice for temporary preservation [24]. When the xenografts had grown for approximately 20 days, the mice were randomized and treated with 5-FU (25 mg kg^{-1}, three times a week, intraperitoneally), RSL3 (100 mg kg^{-1}, twice weekly, intratumorally), teriflunomide (10 mg kg^{-1} in 0.5 % methylcellulose solution, per day, intragastrically), or saline (as a negative control).

For the PDO, surgical specimens were obtained from a 56-year-old female patient diagnosed with sigmoid colon carcinoma who suffered disease progression during neoadjuvant chemotherapy. The third generation of PDO was employed to establish patient-derived organoids-based xenograft (PDOX) models. Female NOG mice, aged 4 weeks, were procured from Weitong Lihua Experimental Animal Technology Company, Ltd. (Beijing). Following a two-week period of adaptive feeding, the 6-week-old mice were utilized as PDOX models. Prior to inoculation, organoids were combined with a high concentration of Matrigel and injected subcutaneously into the mice. Subsequent grouping and treatment protocols mirrored those described above.

2.5. Human studies

The clinicopathological data of the human subjects are provided in Table S1. Patient data and tumor samples were obtained from the Department of Gastrointestinal Surgery, Shandong Provincial Qianfoshan Hospital, and the Department of Colorectal Surgery, Qilu Hospital, Shandong University. The studies were conducted with the written consent of all patients involved and approved by the Shandong Provincial Qianfoshan Hospital for research involving human subjects. The studies were conducted in accordance with the Declaration of Helsinki.

2.6. 5-FU resistant cell line generation

Cells were continuously stimulated by gradually increasing the concentration of 5-FU (from 10^{-8} to 10^{-4} M). As reported previously [19], 5-FU resistance was assessed by determination of the resistance index (RI) after disengaging from 5-FU treatment for 2 weeks. In this study, we used the stably acquired 5-FU-resistant (5FU-R) CRC cell lines HCT8 5FU-R and LoVo 5FU-R as in vitro models.

2.7. Cell viability assay

Cell viability was evaluated using a cell counting kit-8 (CCK-8; MedChemExpress) in accordance with the manufacturer's protocol. Briefly, the cells (5×10^3 cells/well) were seeded in 96-well plates. When the cells reached the right density, they were treated with compounds for the indicated times, after which 10 % (v/v) CCK-8 reagent was added for 0.5–2 h at 37 °C in an incubator. The absorbance value at 450 nm was measured using a microplate reader (Bio-Rad). The relative cell viability was calculated using the following formula: cell viability (%) = (absorbance of treated well - absorbance of blank well)/(absorbance of control well - absorbance of blank well) × 100.

2.8. Triglyceride, phospholipid, cholesterol, and free fatty acid measurements

Cells (1×10^5 cells/well) were seeded in 6-well plates and cultured to approximately 80 % confluency. Samples were extracted with 500 μL isopropanol/n-heptane (1:1, v/v, triglyceride extraction), isopropanol (phospholipid or cholesterol extraction), and n-heptane/methanol/chloroform (24:1:25, v/v/v, free fatty acid extraction). The cells were collected by scraping and prepared for measurement of triglycerides (Solarbio), phospholipids (Abnova), cholesterol (Solarbio), and free fatty acids (Solarbio) using the respective assay kits according to the

manufacturer's protocols. The triglyceride, phospholipid, cholesterol, and free fatty acid concentrations were normalized to the total protein content, and the data are expressed as μmol g^{-1} of protein.

2.9. Metabolomic analysis of medium-chain fatty acids

To determine the composition of intracellular fatty acids, fatty acid metabolites were analyzed by targeted metabolomics. Cells were cultured in 10 cm plates until they reached approximately 80 % confluency. After washing, ice-cold PBS was added to each plate. All of the cells were scraped off the plate and pooled, and 1×10^7 cells per sample were collected for targeted metabolomic analysis of medium-chain fatty acids. The samples were resuspended in glass centrifuge tubes using 1 mL of chloroform/methanol (1:2, v/v) and lysed by sonication. The supernatant was collected, 2 mL of H_2SO_4/methanol solution (1:99, v/v) was added at 80 °C for methyl esterification, and the resulting methyl esters were extracted with 1 mL of hexane. Just before analysis, 25 μL of nonadecanoic acid methyl ester was added as an internal standard to each 500 μL of extracted sample or mixed standard solution.

Gas chromatography-mass spectrometry (GC-MS) was performed using an Agilent 7890 gas chromatograph coupled to an Agilent 5975C mass spectrometer. The chromatography was performed with a high-resolution gas chromatography capillary column (30 m × 0.25 mm i.d) coated with 0.25 μm dimethyl polysiloxane (Agilent Technologies). The temperature was programmed as follows: initial hold at 50 °C for 3 min; gradually increased to 220 °C at a rate of 10 °C/min; and held at 220 °C for 5 min. Helium was used as the carrier gas at a flow rate of 1.0 mL/min. The injection volume was 1 μL, with a split injection ratio of 1:10. To evaluate the stability and reproducibility of the detection system, QC samples (pooled from all samples) were analyzed every five samples. The mass spectrometry conditions were as follows: the injection port, ion source, and transfer line temperature were set to 280, 230, and 250 °C, respectively; the electron bombardment was the electron impact ionization source with 70 eV ionizing energy, in selected ion monitoring scanning mode. The mass data were analyzed using MSD ChemStation software (Agilent Technologies) to extract the chromatographic peak area and retention time. Finally, a standard curve was generated, and the individual fatty acid concentrations of each sample were calculated. The complete platform and fatty acid methyl ester mixed standard solutions were provided by Shanghai Applied Protein Technology Company, Ltd.

2.10. Fatty acid uptake assay

Fatty acid uptake was assessed using the dodecanoic acid fluorescent fatty acid substrate TF2-C12 (Ex/Em = 485/515 nm, Abcam), according to the manufacturer's protocols. Briefly, when the cells in the 6-well plates reached approximately 80 % confluency, they were starved in serum-free medium for 1 h before the assay. The cells were incubated with 1 mL of TF2-C12-loading solution for 1 h and protected from light, harvested by trypsinization, and then resuspended in 500 μL of Hanks balanced buffered saline (HBBS). TF2-C12 uptake was assessed using a FACSAria™ III flow cytometer (BD Biosciences) with a 488 nm laser on the FITC channel. At least 10,000 single cells were recorded per sample, and the raw data were analyzed using FlowJo™ software.

2.11. FAO assay

FAO was measured using FAOBlue (nonanoic acid with blue-fluorescent coumarin derivative modification, Ex/Em = 405/470 nm, Funakoshi) [25]. In brief, cells were cultured in 6-well plates to reach approximately 80 % confluency. The growth medium was then replaced with 10 μM FAOBlue in HBBS and incubated for 1 h. After trypsinization and resuspension, the fluorescence intensity of the released coumarin derivatives was measured using a FACSAria™ III flow cytometer (BD Biosciences). The data collected from 10,000 cells were analyzed using FlowJo™ software.

2.12. Oxygen-consumption rate (OCR) measurement

Oxidation of exogenous fatty acids was assessed by OCR using a Seahorse XFe96 extracellular flux analyzer (Agilent Technologies) as previously described [26]. Cells (2×10^4 per well) were seeded on XFe96 cell culture plates in complete RPMI-1640 medium overnight in a 37 °C incubator. To assess the capacity of the mitochondria to oxidize exogenous fatty acids, the growth medium was replaced with substrate-limited medium (containing 0.5 mM glucose, 1 mM glutamine, 1 % FBS, and 0.5 mM carnitine) and incubated for 24 h. The next day, the Seahorse XF RPMI-1640 assay medium (glucose was added to a final concentration of 2 mM and carnitine was added to a final concentration of 0.5 mM) was replaced, and the plate was left to equilibrate for 1 h in a CO_2-free incubator before assessment. After completion of the pre-treatment, a saturating amount of palmitate-BSA was added to each well and OCR recording began. To assess the capacity of mitochondrial exogenous FAO, cells were treated sequentially with 4 μM etomoxir (an irreversible inhibitor of mitochondrial FAO) and 1 μM FCCP (an uncoupler of mitochondrial oxidative phosphorylation). The OCR of mitochondrial fatty acid oxidation was calculated separately under basal mitochondrial respiration conditions (acute response to etomoxir) and FCCP-induced maximal mitochondrial respiration (maximal response to etomoxir).

Additionally, to evaluate the mitochondrial oxidative capacity of different fatty acids, various fatty acids were added separately to the assay medium, and the OCR was measured before and after etomoxir addition. Fatty acid-dependent OCR was calculated as the difference between before and after etomoxir addition.

2.13. Cellular lipid droplet (LD) measurement

Cells were cultured in 6-well plates until they reached 60 % confluency and then incubated with complete RPMI-1640 medium containing various fatty acids at 100 μM for 24 h. The following day, LDs were identified using the fluorescent neutral lipid dye BODIPY™ 493/503 (Invitrogen). In brief, cells were incubated in 1 mL PBS containing 2 μM BODIPY™ 493/503 for 15 min. The cells were then collected by trypsinization and resuspended in HBBS for LDs measurement. The fluorescence intensity of BODIPY™ 493/503 was assayed using the FACSAria™ III flow cytometer (BD Biosciences) on the FITC channel. A minimum of 10,000 cells were recorded for each sample.

2.14. Malondialdehyde (MDA) measurement

MDA was measured using a colorimetric assay kit (Abcam) according to the manufacturer's protocol. In brief, cells were cultured until they reached 60 % confluency (in 6-well plates) and then incubated with 100 μM DPA or DHA for 24 h. Samples were extracted with 500 μL lysis buffer and then pooled for MDA measurement. The reaction mixture was incubated at room temperature for 30 min. The absorbance of the samples and standards was measured at 695 nm using a microplate reader (Bio-Rad). The MDA levels in the samples were calculated based on a calibration curve generated with standard MDA samples. The final results were normalized to the protein concentration of the cell lysates, and the data were expressed as μmol g^{-1} of protein.

2.15. Lipid peroxidation (LPO) measurement

Lipid peroxidation was measured by directly utilizing redox reactions with ferrous ions, according to the manufacturer's protocol (Abcam). PUFA (DPA, DHA)-treated cells were harvested from 6-well plates. LPO in the samples reacted with Fe^{2+} in the reaction mixture to form the Fe^{3+}, and the resulting Fe^{3+} was detected using SCN^- as the chromogen. The absorbance of the samples and standards was measured

at 500 nm. LPO concentration was normalized to the protein concentration in each well.

2.16. Mitochondrial ultrastructure imaging

After treatment with PUFAs (DPA and DHA), the ultrastructure of the mitochondria was evaluated using transmission electron microscopy (TEM) as previously described. In brief, cells were harvested and fixed for 2 h using 2.5 % (v/v) glutaraldehyde solution at 4 °C. After washing with PBS and centrifugation, the cell mass was pre-embedded in 1 % agarose in an Eppendorf tube. The agarose pre-embedded cells were fixed in 1 % osmium acid for 2 h at room temperature. The samples were then dehydrated using a gradient of alcohol (30 %, 50 %, 70 %, 80 %, 95 %, 100 %, and 100 % alcohol for 20 min at each concentration) and acetone (twice for 15 min each). The dehydrated samples were processed for infiltration and embedding as follows: treatment with acetone:812 embedding agent (1:1) for 4 h at 37 °C; infiltrated with acetone:812 embedding agent (1:2) overnight at 37 °C; and embedded with pure 812 embedding agent for 8 h at 37 °C. The samples were then embedded in embedding molds and placed in a 37 °C oven overnight. The embedding molds were then baked at 60 °C for 48 h to allow polymerization of the embedding resin. The resin sections were cut into 60–80 nm sections using an ultramicrotome (Leica), and the sections were spread flat in 150 mesh cuprum grids with formvar film. The prepared sections were then stained with 2 % uranium acetate-saturated alcohol solution for 8 min and rinsed three times with 70 % ethanol and ultrapure water. The sections were then incubated with 2.6 % lead citrate for 8 min to avoid CO_2 and then rinsed three times with ultrapure water. The dried cuprum grids were imaged using an HT7800 TEM (Hitachi).

2.17. Mitochondrial membrane potential assay

The mitochondrial membrane potential (ΔΨm) was assessed using the fluorescent lipophilic carbocyanine dye JC-1 (MedChemExpress). JC-1 remains monomeric at low ΔΨm, emitting green fluorescence (Ex/Em = 514/529 nm), while JC-1 forms complexes at high ΔΨm, emitting red fluorescence (Ex/Em = 585/590 nm). Cells (1×10^5 per well) were seeded in 24-well plates overnight, and the cells were then treated with 100 μM DPA or DHA for a further 24 h. The cells were then exposed to 2 μM JC-1 (500 μL medium per well) for 20 min in an incubator. After washing the cells three times with PBS, the red and green fluorescence levels were evaluated using an IX73 fluorescence microscope (Olympus).

2.18. Lipid ROS assay

Lipid ROS generation was assessed using C11-BODIPY™ 581/591 (Invitrogen). C11-BODIPY™ 581/591 readily enters cells and exhibits good spectral separation between the non-oxidized (595 nm) and oxidized (520 nm) states. The details of each step are as follows: After overnight culture of 1×10^5 cells per well in 24-well plates, the cells were stimulated for 24 h with DPA or DHA and then labeled with 5 μM C11-BODIPY™ 581/591 for 30 min at 37 °C in an incubator. Fluorescence microscopy (Olympus) was used to image the red and green fluorescence signals.

2.19. Glutathione measurement

Cells (1×10^5 cells/well) were seeded in 6-well plates and cultured until they reached approximately 60 % confluency. The cells were then treated with DHA for 24 h, harvested, and prepared for measurement of reduced and oxidized forms of glutathione (GSH and GSSG, respectively) using a glutathione assay kit (Solarbio) according to the manufacturer's protocols. The reaction results in the formation of a yellow compound (2-nitro-5-thiobenzoate), and the absorbance of the yellow product was measured at a wavelength of 412 nm. Total glutathione and the ratio of GSH and GSSG were calculated based on a standard curve, and the data were normalized to the total protein levels.

2.20. Mitochondrial content measurement

The mitochondria were stained with the potential-dependent fluorescent dye MitoTracker™ Red (Ex/Em = 581/644 nm, Invitrogen). Briefly, cells were cultured in 6-well plates until they reached approximately 80 % confluency. The culture medium was then removed and replaced with 1 mL PBS containing 50 nM MitoTracker™ Red for 30 min at 37 °C. The dye-labeled cells were then harvested and assayed using a FACSAria™ III flow cytometer (BD Biosciences) on the Texas Red channel. At least 10,000 cells were recorded per sample. The data were analyzed using FlowJo™ software, and the geometric mean fluorescence intensity (MFI) was calculated.

2.21. ROS production assay

DCFH-DA (Ex/Em = 488/525 nm) was used for total ROS detection, including OH•, H_2O_2, and peroxy radicals, whereas HKSOX-1m (Ex/Em = 509/534 nm) [27], HKPerox-2 (Ex/Em = 480/527 nm) [28], and HKOH-1r (Ex/Em = 490/520 nm) [29] selectively detect $O_2^{\bullet-}$, H_2O_2, and OH•, respectively. All four probes were purchased from MedChemExpress. Cells were cultured until they reached 80 % confluence in 6-well plates and loaded with 5 μM DCFH-DA, 10 μM HKSOX-1m, 10 μM HKPerox-2, or 5 μM HKOH-1r for 30 min, respectively. The probe-loaded cells were assayed by flow cytometry (BD Biosciences) on the FITC channel, and the data were analyzed using FlowJo™ software. Positive and negative controls were included with each assay.

2.22. Immunocytofluorescence microscopy

Cells (1×10^5 cells per well) were seeded on poly-D-lysine-coated coverslips in 24-well plates overnight. To evaluate the co-localization of mitochondria with glutathione peroxidase 4 (GPX4) or DHODH, mitochondria were labeled with 200 nM MitoTracker™ Green (Invitrogen) for 30 min prior to fixation. The cells were fixed in 4 % paraformaldehyde for 20 min, permeabilized with 0.25 % Triton X-100 for 10 min, and then blocked with 10 % goat serum for 1 h at room temperature while protected from light. The cell coverslips were incubated with antibodies against GPX4 (1:200, ab125066, Abcam) or DHODH (1:100, ab246901, Abcam) overnight at 4 °C. The next day, the bound primary antibodies were detected using CoraLite594-conjugated goat anti-rabbit IgG (H + L) (Proteintech) for 1 h at room temperature. The coverslips were then mounted on slides with mounting medium containing DAPI (Abcam), and the fluorescence signal was imaged using a TCS SP8 confocal laser scanning microscope (Leica).

2.23. Mitochondrial isolation and mitochondrial transplantation

"Donor" cells were seeded in 15 cm plates and cultured until they reached 80 % confluence before mitochondrial isolation. To clearly observe the effect of mitochondrial transplantation, the mitochondria in the donor cells were labeled with 200 nM MitoTracker™ Red (Invitrogen) prior to isolation. Mitochondrial extracts were prepared using a Qproteome® Mitochondria Isolation Kit (Qiagen) in accordance with the manufacturer's protocol. MitoTracker™ Red-labeled cells were washed with ice-cold PBS, trypsinized, and then centrifuged at 500×*g* for 10 min at 4 °C. As much supernatant as possible was removed, and the cell pellet was then carefully washed with ice-cold PBS. The cell pellet was resuspended in 2 mL lysis buffer containing protease inhibitors and slowly shaken for 10 min on ice. The cell lysates were centrifuged at 1000×*g* for 10 min at 4 °C, and the supernatant (which mainly contained cytosolic proteins) and precipitate (which contained the mitochondria) were collected separately. Next, ice-cold disruption

buffer (1.5 mL) was added to the precipitate, and the lysates were homogenized by being passed through a syringe 10 times. The lysates were then centrifuged at 1000×*g* for 10 min at 4 °C, and the supernatant was carefully collected into a 1.5 mL tube. The collected supernatant was immediately centrifuged again at 6000×*g* for 10 min at 4 °C to obtain the mitochondrial pellet. The purified mitochondrial pellet was washed with 1 mL of mitochondrial storage buffer. After washing, the mitochondria were resuspended in 100 μL of mitochondria storage buffer, which was kept at 4 °C and protected from light for transient preservation.

For in vitro mitochondrial transplantation, "acceptor" cells were cultured on 10 cm plates to approximately 80 % confluency, and the mitochondria were labeled with 200 nM MitoTracker™ Green (Invitrogen). After washing, digestion, and resuspension, the acceptor cells (1×10^4 cells/well) were seeded in a 96-well plate and incubated overnight. The next day, the adherent cells were starved in serum-free medium for 2 h before mitochondrial transplantation. The fresh mitochondria were resuspended in Ca^{2+}-free RPMI-1640 culture medium supplemented with 10 % FBS, and the content of mitochondria was adjusted to 20 μg mL^{-1}. After preparation, acceptor cells were incubated with 100 μL of culture medium containing donor mitochondria for 12 h while protected from light in an incubator. After transplantation, the donor mitochondria that were not ingested were removed by washing with PBS. Finally, we observed the mitochondria-transplanted donor cells under a fluorescence microscope (Olympus). Successful mitochondrial transplantation was confirmed by red fluorescence (donor mitochondria) and green fluorescence (acceptor mitochondria) co-occurring in the same cells.

For mitochondrial transplantation in vivo, the coating of purified mitochondria with polymers provided several benefits for mitochondrial transplantation, such as improved biocompatibility, increased stability, and prolonged in vivo retention. Dextran-triphenylphosphonium (TPP) (Qiyuebio) was added to the purified mitochondrial buffer at a final concentration of 5 mg mL^{-1} [30]. Following incubation, washing, and resuspension in mitochondria storage buffer, the dextran-TPP-coated mitochondria were temporarily stored at 4 °C. Intratumoral multiple-point injection (eight points, with a dosage of 200 μg of mitochondria per tumor) was employed for transplantation of the mitochondria.

2.24. Lentivirus-mediated gene knockdown

DHODH short hairpin RNA (sh*DHODH*) sequences specific to *DHODH* were GTGAGAGTTCTGGGCCATAAA (sh$DHODH^{\#1}$) and CGATGGGCTGATTGTTACGAA (sh$DHODH^{\#2}$). sh*DHODH* was cloned into a green fluorescent protein (GFP)-tagged puromycin-inducible lentiviral vector. After lentivirus-mediated sh*DHODH* or negative control (shNC) transfection, green fluorescence and puromycin selection were performed, and the transfection efficiency was verified by real-time quantitative PCR (RT-qPCR) and immunoblotting.

2.25. Transwell® invasion assay

Cell invasion was assessed using Transwell® chambers (8 μm pore size, 24-well, Corning). Matrigel® (BD Biosciences) was thawed on ice and diluted with serum-free RPMI-1640 medium (dilution ratio 1:8). Transwell® chambers were coated with 50 μL diluted Matrigel® and incubated at 37 °C for 1 h. Then, 2×10^5 cells were suspended in 200 μL RPMI-1640 medium with only 0.2 % FBS and added to the upper chamber. In the lower chamber, 600 μL of complete RPMI-1640 medium was added. Following incubation for 24 h, the chambers were fixed with 4 % paraformaldehyde for 20 min and stained with 0.1 % crystal violet solution for 20 min. The cells that did not pass through the membrane were wiped off with a cotton swab, and the cells traversing the membrane were imaged with a microscope (Olympus).

2.26. Colony formation assay

The cell colony formation ability was assessed using a plate-colony formation assay. A total of 700 cells were seeded in 6-well plates with 2 mL of complete RPMI-1640 medium. The medium was changed every three days, and the cells were cultured for a total of 10 days. The clones were fixed with 4 % paraformaldehyde for 20 min, stained with 0.1 % crystal violet solution for 20 min, and then air-dried. A light source underneath the 6-well plates was turned on when the images were captured.

2.27. Wound-healing assay

A wound-healing assay was performed to detect the migration ability of cells in vitro. Cells (1×10^6) were seeded in 6-well plates and incubated overnight. The next day, a dense monolayer of cells had formed, and the cells were scratched using a sterile pipette tip to create a wound. The scratch wounds were imaged with a microscope (Olympus). The cells were cultured in serum-free RPMI-1640 medium for 48 h. The scratch wounds were imaged using a microscope (Olympus). The in vitro migratory ability of the cells was quantified using the wound closure index (%).

2.28. Purification of endogenous human DHODH

The SW620 CRC cell line exhibited a significant level of endogenous DHODH protein expression (Protein Atlas), rendering it suitable for endogenous DHODH purification. Mitochondria were isolated from SW620 cells, and endogenous DHODH was enriched using DHODH antibody-conjugated resins, as described above.

2.29. Expression and purification of truncated Δ29DHODH

An N-terminal deletion was generated in DHODH to eliminate mitochondrial localization and the transmembrane sequence [31]. The cDNA encoding the truncated Δ29DHODH (Met30-Arg396) was amplified by PCR (forward primer: 5′-ACGACAAGCATATGGCCACGGGAGATGAGCG-3′, reverse primer: 5′-GCGACCCGAATTCGGCCGCCGATGATCTGCTCCAATGGC-3′) and subsequently inserted into a pET-19b plasmid. This vector confers ampicillin resistance, an N-terminal His-tag, and regulation of protein expression via isopropyl-β-*d*-thiogalactopyranoside (IPTG). The plasmid pET-19b-Δ29D-HODH was introduced into BL21 (DE3) *Escherichia coli* cells for protein expression following stimulation with 1 μM IPTG (Selleck). The resultant product was Δ29DHODH, which was harvested and purified in accordance with established protocols.

2.30. Mitochondrial DHODH import reaction

The concentrations of $DHODH^{mito}$, $DHODH^{cyto}$, endogenous human DHODH, and Δ29DHODH were determined using an enzyme-linked immunosorbent assay (ELISA). The ELISA plates were coated with antibodies against DHODH (14877-1-AP, Proteintech) for quantitative ELISA, and recombinant human DHODH (rhDHODH, 10062-DD, R&D Systems) was used to generate a standard curve. The DHODH concentrations were adjusted according to the quantitative ELISA results.

DHODH is predominantly localized in the cytosol rather than in the mitochondria in certain fungi (e.g., *Saccharomyces cerevisiae*); thus, mitochondria were isolated from yeast cells for mitochondrial DHODH import reactions. Aliquots of 40 μL of *S. cerevisiae* (Vectorbuilder) in the logarithmic growth phase were collected in an Eppendorf tube, and the mitochondria were extracted from the yeast cells using a yeast mitochondria enrichment kit (Invent) according to the manufacturer's protocol. After the addition of 100 mg of protein extraction powder and 1 mL ice-cold pure water to the tube, the samples were vortexed briefly and centrifuged at 14,000×*g* for 2 min at 4 °C to obtain precipitated

pellets. The yeast pellets were ground using a pestle for approximately 2 min, and 300 μL of buffer A was then added while the grinding was continued for a further 30 s. The tube was immediately vortexed vigorously for 10 s and then centrifuged at 2000×*g* for 2 min at 4 °C to obtain supernatants. The supernatants were then centrifuged at 14,000×*g* for 20 min at 4 °C to obtain a small amount of precipitate. A 200 μL aliquot of buffer B was used to resuspend the precipitate by vortexing, and the tube was then centrifuged at 6000×*g* for 5 min at 4 °C. The supernatant and 1 mL of PBS were mixed in a pre-chilled Eppendorf tube. After thorough mixing, the tube was centrifuged at 16,000×*g* for 30 min at 4 °C, and the yeast mitochondria were enriched in the pellet. The yeast mitochondria were resuspended in 50 μL of mitochondria storage buffer (Qiagen), which was kept at 4 °C for transient preservation.

DHODH import reactions were performed as previously described [32]. The reaction system included 100 μL of buffer solution (600 mM sorbitol, 50 mM HEPES-KOH pH 7.0, 50 mM KCl, 10 mM $MgCl_2$, 2 mM KH_2PO_4, 2.5 mM EDTA, 100 μg fatty acid-free bovine serum albumin, 3 mM NADH, and 1 mM ATP), 50 μg of fresh yeast mitochondria, and 5 μL of lysate containing $DHODH^{mito}$, $DHODH^{cyto}$, endogenous human DHODH, or Δ29DHODH. The reactions took place at 25 °C for 15 min, and the samples were then cooled on ice to terminate the reactions. The mitochondria were collected by centrifugation at 10,000×*g* for 10 min at 4 °C and then resuspended in 50 μL of mitochondrial storage buffer (Qiagen).

2.31. Intramitochondrial localization analysis

To determine the exact intramitochondrial localization of imported DHODH, we used the method reported by Zhuang et al. with a number of modifications [33]. DHODH imported yeast mitochondria were split equally among four groups, and the mitochondria were resuspended in different buffers: isotonic buffer (250 mM sucrose, 10 mM MOPS-KOH pH 7.2, and 1 mM EDTA) without proteinase K; isotonic buffer containing 5 μg mL^{-1} proteinase K; hypotonic buffer (10 mM MOPS-KOH pH 7.2, 1 mM EDTA) containing 5 μg mL^{-1} proteinase K; and hypotonic buffer containing 5 μg mL^{-1} proteinase K and 1 % Triton X-100. After incubation at 4 °C for 15 min, the pellets were collected by centrifugation at 12,000×*g* for 5 min at 4 °C. The harvested pellets were incubated in RIPA buffer containing a protease inhibitor (Roche, Basel, Switzerland), and immunoblotting was then performed. Autophagy-related protein 32 (ATG32, 1:500, CSB-PA340252XA01SVG, Cusabio Technology LCC), coiled-coil-helix-coiled-coil-helix domain containing 4 (CHCHD4, 1:1,000, ARP51896, Aviva), and mitochondrial cytochrome C oxidase II (MTCO2, 1; 500, 4B12A5, Invitrogen) served as the outer mitochondrial membrane (OMM) control, the intermembrane space (IMS) control, and the inner mitochondrial membrane (IMM) control of the yeast mitochondria, respectively.

2.32. DHODH activity measurement

DHODH activity was measured spectrophotometrically by monitoring the decrease in reduced 2,6-dichlorophenol-indophenol (DCPIP) [18]. First, the reaction buffer was prepared, which comprised 50 mM Tris, 150 mM KCl, and 0.1 % Triton X-100, and the pH was adjusted to 8.0. $DHODH^{mito}$, $DHODH^{cyto}$, and endogenous human DHODH were adjusted to a final concentration of 200 ng mL^{-1} in reaction buffer. Additionally, the substrate mixture containing 2 mM DHO, 50 μM DCPIP, 2 μg mL^{-1} rotenone, 2 μg mL^{-1} antimycin A, and 5 mM NaN_3 in reaction buffer was prepared. Then, 50 μL of reaction buffer (blank), 200 ng mL^{-1} endogenous human DHODH (positive control), 200 ng mL^{-1} endogenous human DHODH with 500 μM brequinar (negative control), 200 ng mL^{-1} $DHODH^{Mito}$, or 200 ng mL^{-1} $DHODH^{Cyto}$ were added to 96-well plates. The 96-well plates were placed in a microplate reader (Bio-Rad), and the absorbance values of the samples and controls were measured at 600 nm for 5 min in kinetic mode. The DHODH activity was indirectly calculated based on the reduction of DPIP.

2.33. N-terminal sequence analysis of $DHODH^{Mito}$ and $DHODH^{Cyto}$

DL-dithiothreitol solution was added into the protein solution to a final concentration of 10 mmol/L and incubated in a 56 °C water bath for 1 h. Subsequently, iodoacetamide solution was added to a final concentration of 50 mmol/L and shielded from light for 40 min. Enzyme was then introduced into the protein solution, which was allowed to incubate at 37 °C overnight. Following digestion, the peptide underwent desalting using a self-priming desalting column, with solvent evaporation carried out in a vacuum centrifuge at 45 °C. The peptide was solubilized in the sample solution containing 0.1 % formic acid and 2 % acetonitrile, followed by vigorous vortexing, centrifugation at 13200 rpm for 10 min at 4 °C, and subsequent transfer of the supernatant to a sample tube for mass spectrometry analysis.

The Nano LC-MS/MS analysis was conducted using the Easy-nLC 1200 system (ThermoFisher) and Q Exactive™ Hybrid Quadrupole-Orbitrap™ Mass Spectrometer (ThermoFisher). Subsequently, the raw MS files were subjected to analysis and searched against a target protein database specific to the species of the samples utilizing the Byonic software. The experimental conditions were defined as follows: protein modifications included carbamidomethylation (C) (fixed), oxidation (M) (variable), and acethylation (N-term) (variable); enzyme specificity was designated as Chymotrypsin and Asp-N; the maximum allowed missed cleavages were limited to 3; the precursor ion mass tolerance was set at 20 ppm, with a MS/MS tolerance of 0.02 Da. Peptides identified with high confidence were selected for subsequent protein identification analysis.

2.34. Metabolomic analysis of nucleotides and related substances

The concentrations of intracellular nucleotides and related substances were determined using ultra-high-pressure liquid chromatography-coupled tandem mass spectrometry (UHPLC-MS/MS). Cells were cultured in 6-well plates until they reached approximately 80 % confluency, at which point they were treated with or without 10 μM 5-FU for 12 h. A total of 1×10^6 cells were then collected and suspended in a solution consisting of 80 % methanol. The suspension was subjected to five cycles of ultra-sonication while in an ice-water bath. The cell mixture was then placed at −20 °C for 30 min, followed by centrifugation at 4 °C and 15,000×*g* for 15 min. The resulting cell-free supernatant was evaporated to dryness and then reconstituted in 40 μL of a solution composed of 50 % acetonitrile. The reconstituted samples were subjected to UHPLC-MS/MS analysis.

The UHPLC-MS/MS analysis was conducted using an Agilent 1290 Infinity II UHPLC system coupled to a 6470A Triple Quadrupole mass spectrometer. The samples were injected into a Waters BEH Amide column at a flow rate of 0.25 mL/min. The mobile phase consisted of two components: (A) water with 15 mM ammonium acetate at pH 8.5 and (B) 90 % acetonitrile. The eluted analytes underwent ionization by utilization of an electrospray ionization source in positive mode (ESI−). The ESI−source drying gas and sheath gas were maintained at temperatures of 300 and 350 °C, respectively. The flow rates of the ESI source drying and sheath gases were set to 5 and 11 L/min, respectively. The nebulizer pressure was set at 40 psi, and the capillary voltage was set at 4000 V. To obtain data in an optimized multiple reaction monitoring (MRM) transition, dynamic MRM was employed. The instruments were controlled, and data acquisition was performed using MassHunter software (version B.08.00, Agilent).

2.35. RNA extraction and quantitative PCR

Total RNA from 2×10^6 cells was extracted with 1 mL of TRIzol® reagent (Invitrogen), and the RNA concentration was measured using a NanoDrop™ spectrophotometer (NanoDrop Technologies). cDNA was

generated using 1000 ng of isolated RNA as the template with a ReverTra Ace™ qPCR RT kit (Toyobo) for the reverse transcriptase reaction. The RT-qPCR reaction system included 5 μL of SYBR™ Green Real-Time PCR Master Mix (Toyobo), 0.8 μL gene-specific primers, 3.2 μL sterile RNAse-free water, and 1 μL cDNA using a LightCycler® 480 II instrument (Roche). The threshold cycle (Ct) values of genes were normalized to the housekeeping gene *ACTB*, and relative mRNA quantification was performed by the $2^{-\Delta\Delta Ct}$ method. The primer information is shown in Table S2.

2.36. PCR array of nucleotide metabolism gene expression

Nucleotide metabolism-related gene expression profiling was performed using a 96-well human nucleotide metabolism collection panel PCR array (WcGene). The list of genes is presented in Table S3. RNA extraction and cDNA synthesis were performed as described previously. The diluted cDNA and SYBR™ Green qPCR mix were added to the PCR array. The PCR was performed using a LightCycler® 480 II instrument (Roche, Basel, Switzerland). The threshold cycle (Ct) values of the genes were normalized to *ACTB*, and relative mRNA quantification was determined using the $2^{-\Delta\Delta Ct}$ method.

2.37. Protein extraction and immunoblotting

Total protein was extracted using RIPA lysis buffer (Thermo Scientific) containing a protease inhibitor (Roche) and a phosphatase inhibitor (Roche). The protein lysates were sonicated and clarified by centrifugation. The protein concentration was determined using a bicinchoninic acid (BCA) assay kit (Thermo Scientific) using a microplate reader (Bio-Rad) at a wavelength of 562 nm. The 5 × protein loading buffer (Beyotime) was added to the lysates, and the final mixtures were heated to 98 °C for 10 min. WB was performed as previously described. Electrophoresis was performed using 10 % (v/v) sodium dodecyl sulfate-polyacrylamide gel electrophoresis (SDS-PAGE) gels (Bio-Rad), and the electrophoresed proteins were transferred to 0.45 μm polyvinylidene difluoride (PVDF) membranes (Millipore). The membranes were blocked for 1 h with blocking buffer (containing 5 % skim milk powder) at room temperature and then incubated with primary antibody overnight at 4 °C. The primary antibodies used in immunoblotting included anti-FATP4 (1:2,000, ab199719, Abcam), anti-FABP1 (1:5,000, ab171739, Abcam), anti-CD36 (1:1,000, ab252922, Abcam), anti-FASN (1:2,000, ab128856, Abcam), anti-CPT1A (1:2,000, 15184-1-AP, Proteintech), anti-CPT2 (1:2,000, 26555-1-AP, Proteintech), anti-ACOX1 (1:4,000, 10957-1-AP, Proteintech), anti-caspase-3 (1:1,000, 9662, Cell Signaling), anti-cleaved caspase-3 (1:1,000, 9661, Cell Signaling), anti-SLC7A11 (1:4,000, ab175186, Abcam), anti-GPX4 (1:2,000, ab125066, Abcam), FSP1 (1:2,000, ab197896, Abcam), anti-GCH1 (1:2,000, ab236387, Abcam), anti-DHODH (1:1,000, ab246901, Abcam), anti-NDUFB8 (1:5,000, ab192878, Abcam), anti-SDHB (1:50,000, ab175225, Abcam), anti-UQCRC2 (1:2,000, 14742-1-AP, Proteintech), anti-MTCO1 (1:1,000, ab14705, Abcam), anti-ATP5A (1:2,000, ab176569, Abcam), anti-CAD (1:500, 16617-1-AP, Proteintech), and anti-TS (1:2,000, 15047-1-AP, Proteintech). Additionally, β-Actin (1:10,000, 81115-1-RR, Proteintech), α-Tubulin (1:20,000, 66031-1-Ig, Proteintech), and VDAC (1:1,000, 10866-1-AP, Proteintech) were used as internal references. The bound primary antibodies were then detected using goat anti-rabbit/mouse IgG (H + L) horse radish peroxidase (HRP)-conjugated secondary antibodies (Proteintech) and chemiluminescence-based imaging (Millipore).

2.38. Histology and immunohistochemistry

Fresh tumor samples were embedded in paraffin sections, as previously described. Briefly, tissues were trimmed with a scalpel and fixed in 10 % neutral-buffered formalin for at least 24 h. The tissues were then placed in an embedding box and transferred to a dehydrator (Diapath). Dehydration was performed as follows: 75 % ethanol for 4 h, 85 % ethanol for 2 h, 90 % ethanol for 2 h, 95 % ethanol for 1 h, anhydrous ethanol (I) for 30 min, anhydrous ethanol (II) for 30 min, benzene alcohol for 10 min, xylene (I) for 10 min, and xylene (II) for 10 min. The embedding box was then placed in melted paraffin (65 °C), with three changes of 1 h each. The wax-soaked tissues were embedded in an embedding machine (Leica). The resulting paraffin blocks were cooled with a −20 °C freezing table and trimmed for sectioning. Finally, 5 μm sections were cut using a microtome (Leica), flattened on the 40 °C warm water of the spreading machine (Leica), and then picked up by the glass slides.

For histological and immunohistochemical staining, paraffin sections were dewaxed as follows: environmental protection dewaxing liquid for three changes of 15 min each, 100 % ethanol for 5 min, 95 % ethanol for 5 min, 85 % ethanol for 5 min, and 75 % ethanol for 5 min, and then rinsed with pure water. Hematoxylin and eosin (H&E) staining was used to evaluate tumor morphology. The sections were stained with hematoxylin solution (Beyotime) for 3 min and then rinsed with tap water. The sections were then stained with eosin dye (Beyotime) for 5 min after ethanol gradient dehydration. Immunohistochemistry (IHC) was performed to localize specific tissue antigens. Sections were submerged in 0.01 M citric acid antigen repair solution (pH 6.0) and repaired in a microwave oven. The sections were then placed in 3 % hydrogen peroxide to block endogenous peroxidase activity, followed by incubation with 10 % goat serum for 1 h to prevent nonspecific binding. The following primary antibodies were incubated overnight at 4 °C: anti-Ki67 (1:1,000, ab15580, Abcam), anti-cleaved caspase-3 (1:400, 9661, Cell Signaling), anti-4-HNE (1:25, ab48506, Abcam), anti-adipophilin (1:100, ab270274, Abcam), and anti-DHODH (1:50, ab246901, Abcam). The sections were then incubated with HRP-conjugated anti-rabbit/mouse IgG (Zhongshan Golden Bridge), and the antigen signal was developed by 3,3′-diaminobenzidine (DAB) staining (Zhongshan Golden Bridge). Nuclei were counterstained with hematoxylin solution (Beyotime) for 3 min followed by rinsing with tap water. The sealed slides were imaged using an Axio Scope A1 microscope (Zeiss).

2.39. Statistical analysis

The statistical analyses were conducted using GraphPad Prism 8, employing the two-tailed Student's *t*-test, one-way analysis of variance (ANOVA), or two-way ANOVA. Survival curves were generated using the Kaplan–Meier method. The data are presented as mean ± standard deviation (SD). Statistical significance was denoted by * $P < 0.05$, ** $P < 0.01$, and *** $P < 0.001$, and ns indicated no significance. The cell culture experiments were conducted with a minimum of three independent replicates. At least five animals were included in each experimental group. The statistical details are included in the respective figure legends.

3. Results

3.1. Excessive lipid accumulation of 5-FU-resistant (5FU-R) CRC cells

Dysfunctional lipid metabolism during tumor initiation and progression has drawn increasing attention in recent years [34,35]. To examine the lipid metabolic profiles associated with 5-FU resistance, we established models of acquired 5-FU resistance in CRC cell lines (HCT8 and LoVo) [19] by subjecting WT CRC cells to increasing concentrations of 5-FU for approximately 8 months. When the treatment regimen concluded, the resulting 5FU-R CRC cell lines exhibited a resistance level approximately 500-fold greater than that of WT cells (Fig. S1A, **1A**, S1B). We first compared the lipid content and observed that 5FU-R CRC cells exhibited higher abundances of triglyceride, phospholipid, cholesterol, and free fatty acids than WT cells (Fig. 1B). Gas chromatography-mass spectrometer (GC-MS) was conducted to quantify

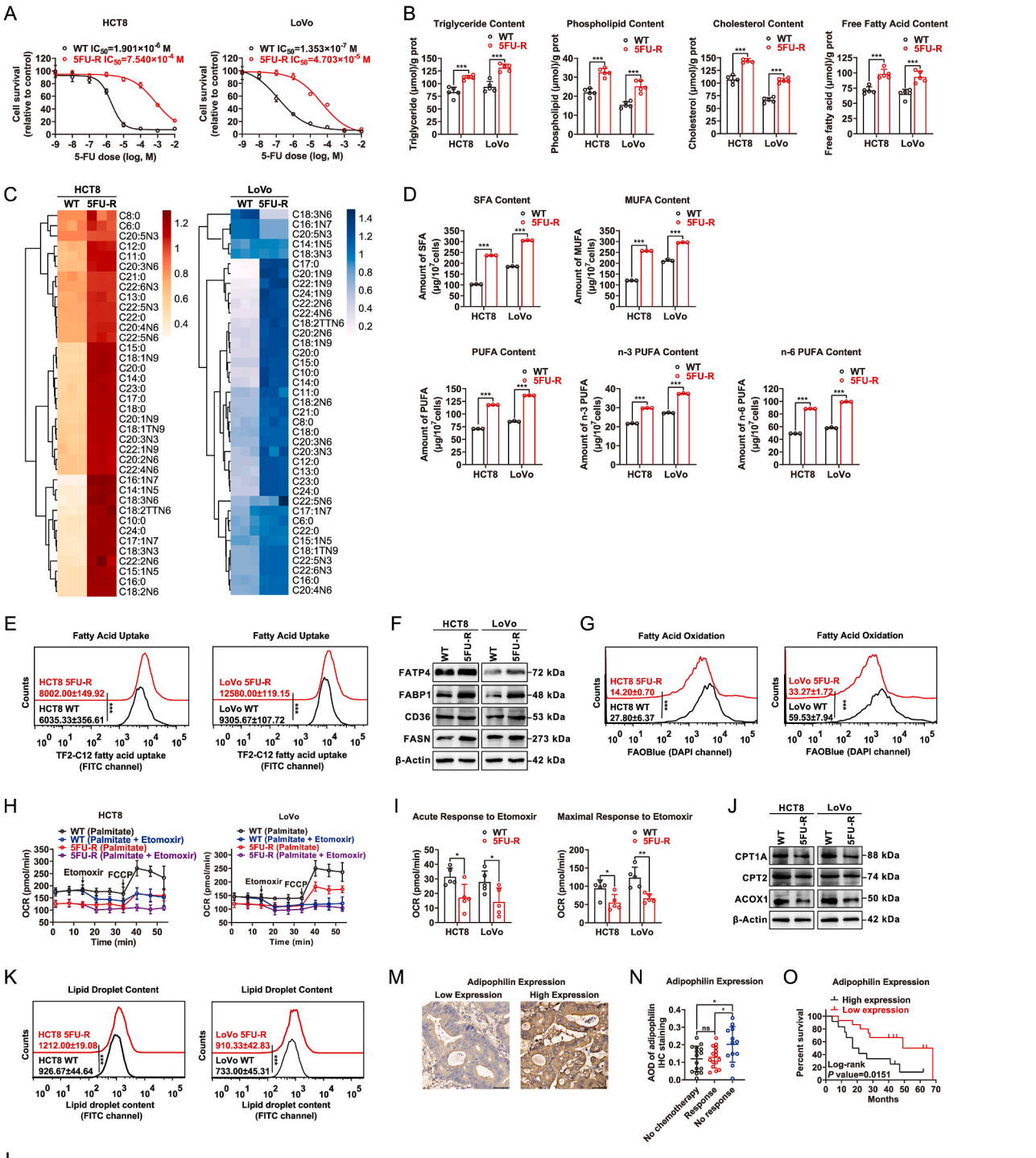

(caption on next page)

Fig. 1. Lipid metabolism reprogramming of 5FU-R CRC cells
A. Cell survival in 5FU-R and corresponding control cells treated with increasing concentrations of 5-FU for 72 h
B. Triglycerides, phospholipids, cholesterol, and free fatty acid content in 5FU-R and corresponding WT cells. The values were normalized with the total protein concentration.
C. Heatmaps comparing captured fatty acids from 5FU-R and corresponding WT cells.
D. The amount of SFAs, MUFAs, and PUFAs (n-3 and n-6) in 5FU-R and corresponding WT cells, based on the metabolomic data.
E. Flow cytometric histogram of the fluorescence intensity (FITC channel) in 5FU-R and corresponding WT cells upon staining with TF2-C12-loading solution for 1 h
F. Protein expressions of FATP4, FABP1, CD36, and FASN in the indicated cancer cells. β-actin served as an internal reference.
G. Flow cytometric histogram of the fluorescence intensity (DAPI channel) in 5FU-R and corresponding WT cells upon treatment with FAOBlue (10 μM) for 1 h
H. OCR was measured in a medium saturated with palmitate-BSA, and subsequently subjected to sequential exposure of etomoxir (4 μM) and FCCP (1 μM).
I. Comparing acute response and maximal response to etomoxir for assessing the mitochondrial FAO capacity.
J. Protein expressions of CPT1A, CPT2, and ACOX1 in the indicated cancer cells. β-actin served as an internal reference.
K. Flow cytometric histogram of the fluorescence intensity (FITC channel) in 5FU-R and corresponding WT cells upon staining with BODIPY 493/503 (2 μM) for 15 min.
L. The CRC cohort included three clinical therapy subcohorts: No chemotherapy group, Response group, No response group. Clinical parameters are indicated in the heatmap.
M. Representative images of IHC staining for adipophilin on tumor sections in CRC patients, scale bar = 50 μm
N. Comparison of IHC staining (AOD) for adipophilin in three CRC subcohorts.
O. Kaplan–Meier survival curves of disease-free survival of CRC patients on fluorouracil analog-based chemotherapy with high (AOD $\geq$0.15, n = 12) or low (AOD $<$0.15, n = 15) adipophilin expression as assessed by the IHC images.
Data are shown as means ± SD. The statistical analyses were performed using the unpaired Student's *t*-test or ANOVA, and survival was compared by log rank (Mantel–Cox) testing. $^{*}P < 0.05$, $^{**}P < 0.01$, $^{***}P < 0.001$, or ns = not significant. SD, standard deviation; ANOVA, analysis of variance; CRC, colorectal cancer; 5FU-R, 5-fluorouracil-resistant; SFA, saturated fatty acid; MUFA, monounsaturated fatty acid; PUFA, polyunsaturated fatty acid; FCCP, ionophore uncoupler trifluorocarbonylcyanide phenylhydrazone; IHC, immunohistochemistry; FASN, fatty acid synthase; FAO, fatty acid oxidation.

the proportions of saturated fatty acids (SFAs), monounsaturated fatty acids (MUFAs), or PUFAs among all free fatty acids. The results indicated that all fatty acid fractions exhibited greater accumulation in 5FU-R CRC cells than in WT cells (Fig. 1C, D, S1C).

To investigate the mechanisms underlying fatty acid accumulation in 5FU-R CRC cells, we evaluated fatty acid uptake, de novo synthesis, and oxidation. Our findings indicated that the exogenous uptake of fatty acids was augmented (Fig. 1E), and the expression levels of critical fatty acid transporters, including fatty acid transport protein 4 (FATP4), fatty acid binding protein 1 (FABP1), and CD36, were significantly upregulated in 5FU-R CRC cells compared with those of WT cells (Fig. 1F–S1D). We also observed significant upregulation of the level of fatty acid synthase (FASN), a key enzyme in the process of fat synthesis, in 5FU-R CRC cells (Fig. 1F–S1D). In addition, a range of methods were employed to evaluate the FAO capacity of 5FU-R CRC cells compared with that of WT cells. These findings revealed a reduced FAO capacity (Fig. 1G), diminished mitochondrial reserve FAO capacity (Fig. 1H and I), and suppressed expression of FAO enzymes (Fig. 1J–S1E), suggesting a possible impairment of the mitochondrial respiratory capacity. The regulatory organelles for cellular lipid metabolism are lipid droplets (LDs) in which excess lipids are stored [36]. We compared the LD content between the cell models and patient specimens. Our findings indicated a significant increase in the number of LDs in 5FU-R CRC cells compared with that in WT cells (Fig. 1K). Consistently, higher levels of adipophilin, a molecular label on the LD surface [37], were observed in the non-response group (poor response to preoperative fluorouracil analog-based chemotherapy) than in the other groups (Fig. 1L–N). Furthermore, patients with CRC who underwent preoperative fluorouracil analog-based chemotherapy and exhibited high adipophilin expression experienced poor disease-free survival after surgery compared with those with low adipophilin expression, irrespective of their response status (Fig. 1O). These findings suggest that an imbalance in the uptake, synthesis, and oxidation of fatty acids may contribute to metabolic disorders and excessive lipid accumulation in 5FU-R CRC. Notably, excessive lipid accumulation appears to be linked to 5-FU resistance and a negative prognosis in CRC.

3.2. PUFAs Preferentially accumulate into LDs in 5FU-R CRC cells

Fatty acids constitute a class of compounds with a wide range of biological activities. In this study, we conducted a comparative analysis of the ability of 5FU-R CRC cells and corresponding WT cells to capture and store various types of fatty acids in LDs, including SFAs such as PA, MUFAs such as OA, omega-6 (n-6) PUFAs such as LA, ARA, and DPA, and omega-3 (n-3) PUFAs such as ALA, EPA, and DHA (Fig. 2A). LD accumulation of all fatty acids was greater in 5FU-R CRC cells than in WT cells (Fig. 2B, **S2A**). Notably, the capacity for LD formation increased in proportion with the number of unsaturated bonds upon exogenous administration of n-6 PUFAs (C18:2, LA < C20:4, ARA < C22:5, DPA) and n-3 PUFAs (C18:3, ALA < C20:5, EPA < C22:6, DHA) (Fig. 2B–S2A). In addition to assessing the uptake and accumulation of the fatty acids, we measured oxidation using various types of fatty acids. The oxygen-consumption rate (OCR) in response to various fatty acids was notably diminished in 5FU-R CRC cells compared to that in WT cells (Fig. 2C–S2B). Moreover, the oxidative capacity of PUFAs was inferior to that of SFAs and MUFAs and the quantity of unsaturated bonds in PUFAs was inversely correlated with their oxidative capacity (Fig. 2C–S2B). Taken together, these data provide compelling evidence that PUFAs exhibit a predilection for accumulation within the LDs of 5FU-R CRC cells, and the degree of unsaturation may play a role in the storage of LDs.

3.3. PUFAs exert cytotoxic effects and increase chemosensitivity in 5FU-R CRC cells

Notably, exposure to fatty acids resulted in significant inhibition of 5FU-R CRC cell growth under certain circumstances, while no such effect was observed in the corresponding WT cells. Thus, a series of experiments was conducted to examine the potential cytotoxic effects of various concentrations and durations of fatty acid exposure. The results indicated that SFA and MUFA exposure did not significantly impede cell growth, whereas PUFAs exhibited dose- and time-dependent inhibition of cell growth in 5FU-R CRC cells, but not in their corresponding WT cells (Figs. S3A and B). The cytotoxic effects of n-6 and n-3 PUFAs were directly proportional to the number of unsaturated bonds (Figs. S3A and B). Furthermore, 3D cell culture was used to examine the cytotoxic effects of PUFAs and their effect on chemotherapy efficacy. Within the 3D spheroids, exogenous SFAs and MUFAs did not appear to affect growth in either 5FU-R or WT CRC cells, whereas the cytotoxic effects of PUFAs were proportional to the number of unsaturated bonds in 5FU-R CRC cells from 3 to 6 days post-exposure (Fig. 2D, **S4A**). 5FU-R CRC cells also displayed significant resistance in the 3D culture environment when treated with 5-FU. Notably, the co-administration of 5-FU and PUFAs elicited a remarkable synergistic effect, particularly with DPA and DHA,

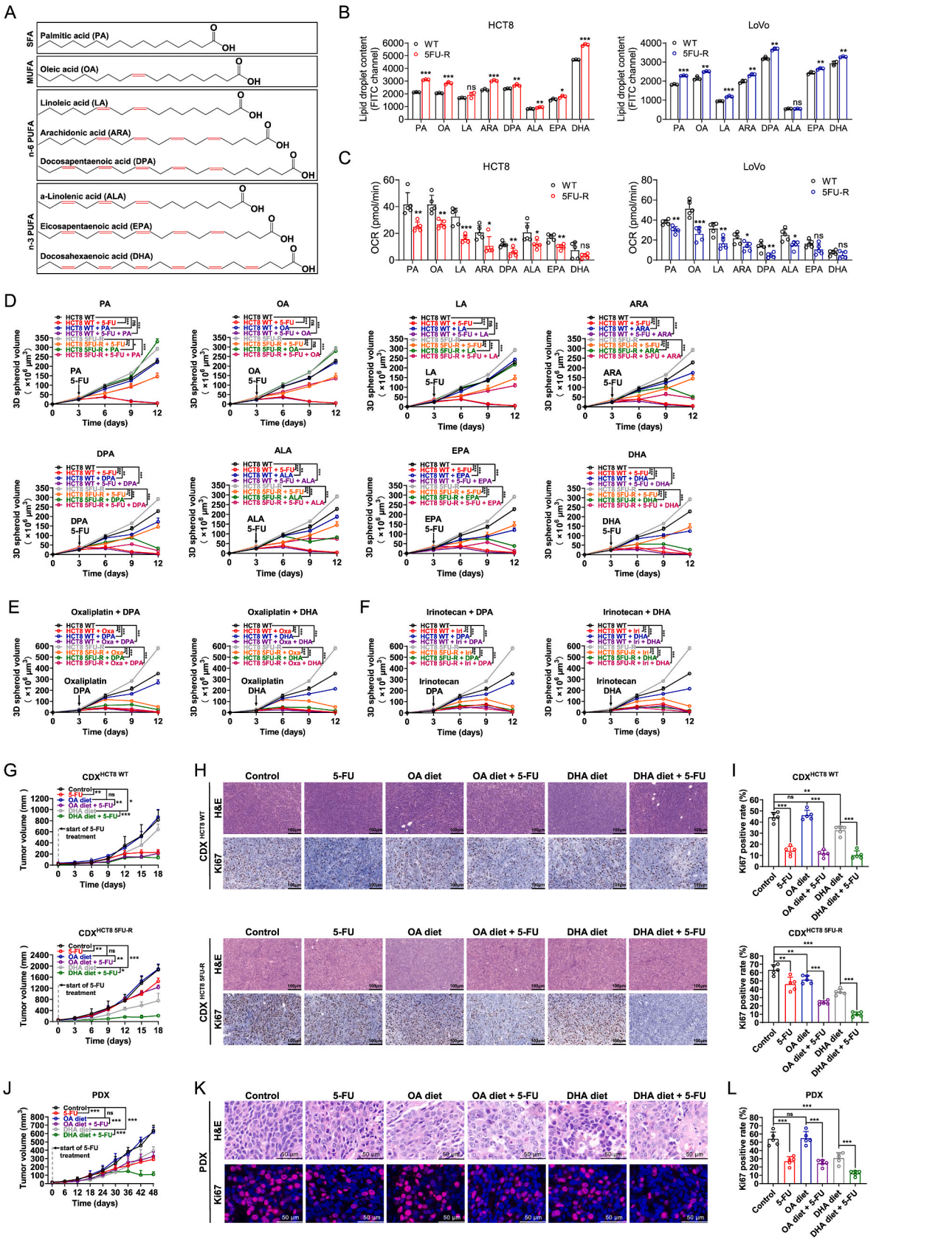

(caption on next page)

Fig. 2. Accumulated PUFAs exert cytotoxic effects on 5FU-R CRC cells
A. Structural formulas of representative SFA, MUFA, n-6 PUFA, and n-3 PUFA.
B. Flow cytometric statistical analysis of the fluorescence intensity (FITC channel) in 5FU-R and corresponding WT cells stained with BODIPY 493/503 (2 μM) for 15 min to 100 mM FAs including PA, OA, LA, ARA, DPA, ALA, EPA, and DHA.
C. Effects of the 100 μM indicated FAs on the OCR in 5FU-R and corresponding WT cells. OCR was measured in a medium with 100 μM indicated FAs, and subsequently subjected to etomoxir (4 μM).
D–F. Effects of the indicated FAs and chemotherapeutic agents on the growth of 3D tumor spheroids generated from 5FU-R cells and their WT counterparts. Indicated FAs and chemotherapeutic agents were introduced starting from day three and replaced every three days. **(D)** Indicated FAs (100 μM) or 5-FU (10 μM), **(E)** PUFAs (100 μM) or oxaliplatin (1 μM), and **(F)** PUFAs (100 μM) or irinotecan (50 μM)
G. Tumor volumes of WT and 5FU-R HCT8 xenografts with the indicated diets and 5-FU treatment at different time points (days).
H, I. (H) Representative images of H&E staining and Ki67 IHC staining on WT and 5FU-R HCT8 xenograft tumor sections with the indicated diets and 5-FU treatment, scale bar = 100 μm. **(I)** Ki67 positive rates in the indicated xenograft tumors.
J. Tumor volumes in the PDX model with the indicated diets and 5-FU treatment at different time points (days).
K, L. (K) Representative images of H&E staining and Ki67 IF staining of PDX tumor sections with the indicated diets and 5-FU treatment. DAPI (blue), Ki67 (red), scale bar = 50 μm. **(L)** Ki67 positive rates in the indicated PDX tumors.
Data are shown as mean ± SD. The number of mice in each group was five. The statistical analyses were performed using the unpaired Student's *t*-test or ANOVA. $^{*}P < 0.05$, $^{**}P < 0.01$, $^{***}P < 0.001$, or ns = not significant. SD, standard deviation; ANOVA, analysis of variance; CRC, colorectal cancer; 5FU-R, 5-fluorouracil-resistant; SFA, saturated fatty acid; MUFA, monounsaturated fatty acid; PUFA, polyunsaturated fatty acid; IHC, immunohistochemistry; PA, palmitic acid; OA, oleic acid; LA, linoleic acid; ARA, arachidonic acid; DPA, docosapentaenoic acid; ALA, alpha-linolenic acid; EPA, eicosapentaenoic acid; DHA, docosahexaenoic acid; PDX, patient-derived xenograft. (For interpretation of the references to color in this figure legend, the reader is referred to the Web version of this article.)

which both contain a greater number of unsaturated bonds (Fig. 2D–S4A). Additionally, 5FU-R CRC cells were resistant to other chemotherapeutic agents such as oxaliplatin and irinotecan in 3D culture, and the results of the combined treatment of chemotherapy plus PUFAs was superior to the use of both reagents separately in 5FU-R CRC cells (Fig. 2E, F, S4B, C).

To assess the impact of PUFAs in vivo, mice were fed standard rodent, OA-enriched, or DHA-enriched diets. Subsequently, CDX and PDX models were established, wherein mice were transplanted with HCT8 WT cells ($CDX^{HCT8\ WT}$), HCT8 5FU-R cells ($CDX^{HCT8\ 5FU-R}$), 5-FU-resistant tumor fragment (PDX^{5FU-R}), or 5-FU-resistant organoid ($PDOX^{5FU-R}$) 2 weeks after the respective diets had commenced. Mice were then injected with either 5-FU or saline (negative control) following the detection of measurable tumors. The PUFA-rich diet significantly delayed the growth of 5-FU-resistant CRC tumors ($CDX^{HCT8\ 5FU-R}$, PDX^{5FU-R}, and $PDOX^{5FU-R}$ models) compared with the control or MUFA-rich diet (Fig. 2G–L, S4D–M). Notably, combined treatment with DHA and 5-FU, but not either treatment alone, strongly suppressed the growth of 5-FU-resistant CRC tumors (Fig. 2G–L, S4D–M), which is consistent with our in vitro data (Fig. 2D).

3.4. Cytotoxic effects of PUFAs in 5FU-R CRC cells result from ferroptosis

According to recent research, PUFAs can selectively induce cancer cell death under ambient acidosis [26]. Thus, we utilized a medium buffered at a higher pH and observed the nullification of the cytotoxic effects of both DPA and DHA. This suggests that the observed anticancer effects cannot be attributed to acidosis (Fig. 3A). The process of cell death involves intricate signaling cascades and molecular effector mechanisms [38]. Presently, the focus is primarily on the four distinct forms of active cell death: apoptosis, necroptosis, pyroptosis, and ferroptosis [38] (Fig. 3B). Caspase 3 serves as a crucial mediator of apoptosis; however, the process of cell death induced by PUFAs does not entail caspase 3 cleavage (Fig. 3C). Similarly, the co-administration of PUFAs and a necroptosis inhibitor necrostatin-1 to 5FU-R CRC cells demonstrated that PUFA-induced cell death is distinguishable from necroptosis (Fig. 3D). As pyroptosis is a highly inflammatory cell death pattern, it was excluded from this study. Importantly, the administration of ferroptosis inhibitors (ferrostatin-1 or liproxstatin-1) resulted in near-complete inhibition of cell death caused by PUFAs (Fig. 3E). In vivo, a PUFA-rich diet resulted in a significant increase in 4-HNE (a LPO marker) expression in $CDX^{HCT8\ 5FU-R}$ tumors, as opposed to caspase 3 cleavage (Fig. 3F and G). Collectively, these results suggest that the cytotoxic effects of PUFAs on 5FU-R CRC cells are attributable to ferroptosis.

A fundamental target of chemotherapy is the activation of endocellular signaling mechanisms involved in cell death pathways; thus, we further assessed the effect of cell death pathway blockade on chemosensivity of CRC cells. WT and 5FU-R CRC cells were treated with ferrostatin-1, z-VAD-fmk, or necrostatin-1 to inhibit specific death pathways before exposure to varying concentrations of 5-FU. Inhibition of ferroptosis was found to significantly reduce 5-FU sensitivity in both WT and 5FU-R cells (Fig. S5A), while z-VAD-fmk and necrostatin-1 showed a minor decrease in sensitivity, although no statistically significant difference in IC_{50} was observed (Figs. S5B and C). Moreover, the combination of 5-FU and ferrostatin-1 was employed in the 5-FU sensitive PDX model, revealing that suppression of ferroptosis resulted in reduced sensitivity to 5-FU (Figs. S5D–F).

Next, to further investigate the role of ferroptosis in PUFA-induced cell death, both 5FU-R and WT CRC cells were exposed to PUFAs, and the level of MDA production was assessed, as the accumulation of MDA serves as a hallmark of ferroptosis. The results revealed a significant increase in the MDA levels in 5FU-R CRC cells in the presence of DPA and DHA (Fig. 3H). Moreover, using redox reactions with ferrous ions as direct indicators of LPO, we observed elevated levels of LPO in 5FU-R CRC cells following PUFA treatment (Fig. 3I). Subsequently, TEM was used to verify that 5FU-R CRC cells underwent ferroptosis following treatment with PUFAs. This was indicated by the small mitochondria that possessed augmented membrane density, diminished mitochondrial cristae, and the presence of vacuoles (Fig. 3J). JC-1 staining revealed that the mitochondrial membrane potential was disrupted by PUFAs in 5FU-R CRC cells (Fig. 3K). Given the close association between lipid reactive oxygen species (ROS) and ferroptosis [17], we aimed to determine whether PUFAs induce lipid ROS production. Our findings revealed a higher accumulation of lipid ROS in 5FU-R CRC cells than in WT cells (Fig. 3L).

3.5. Ferroptosis as a vulnerability in 5FU-R CRC cells

As previously described, PUFAs were observed to act as inducers of ferroptosis, resulting in the death of 5FU-R CRC cells without significantly affecting corresponding WT cells. This difference may be attributed to the vulnerability of 5FU-R CRC cells to ferroptosis. Further, the sensitivity of 5FU-R CRC cells to ferroptosis induced by a class 2 ferroptosis inducer (RSL3, which inhibits GPX4 activity) or a class 1 ferroptosis inducer (erastin, which blocks SLC7A11-mediated cystine transport) was significantly greater than that of WT cells (Fig. 4A and B). This effect was completely rescued by the ferroptosis inhibitor, liproxstatin-1 (Fig. 4A and B). Additionally, 3D cell culture was used to investigate the effects of ferroptosis inducers on the efficacy of chemotherapy. The results demonstrated that RSL3 significantly inhibited the proliferation of 5FU-R 3D spheroids, and coadministration of RSL3 and

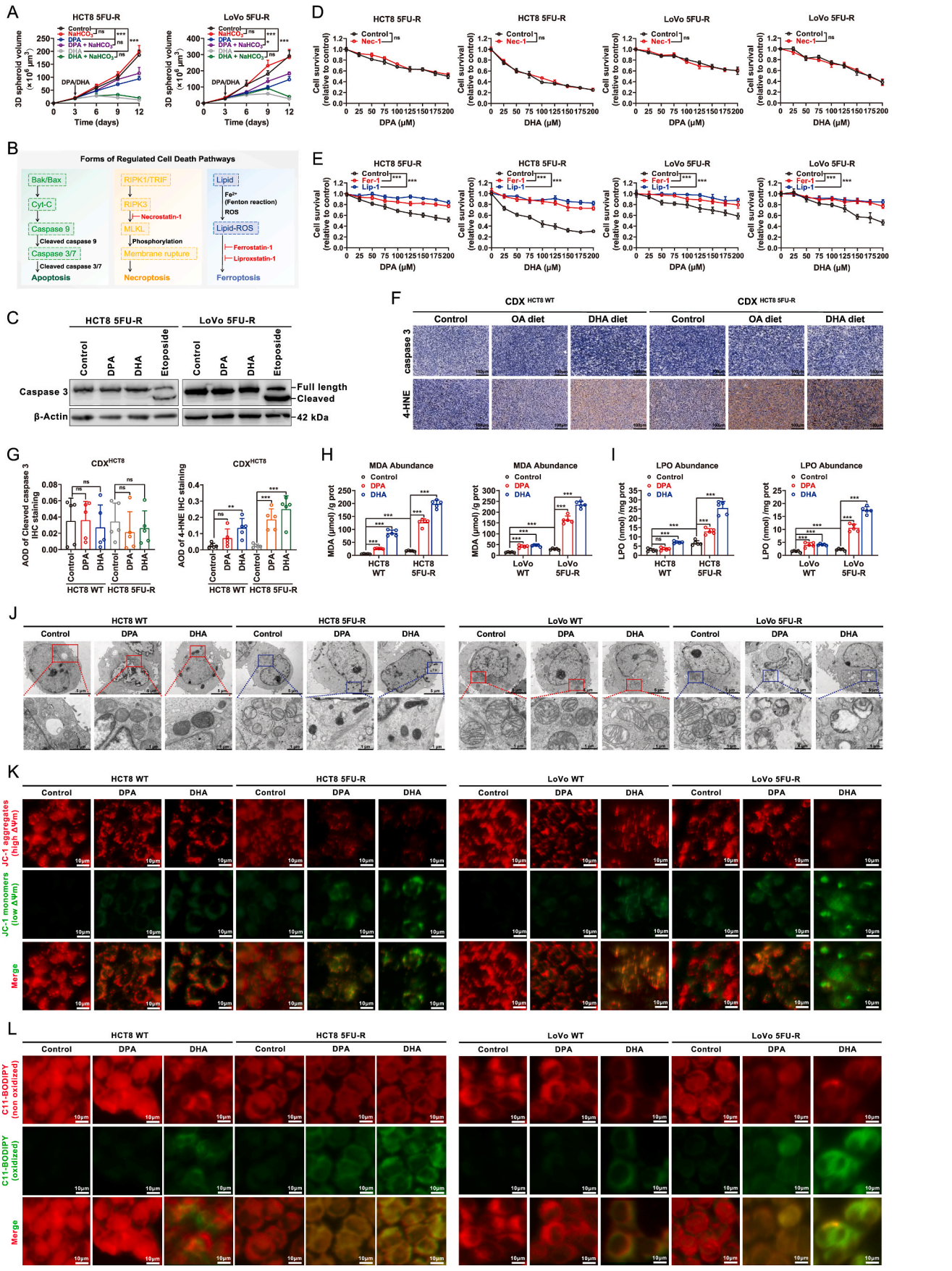

(caption on next page)

Fig. 3. Exogenous PUFAs lead to ferroptosis-induced cell death in 5FU-R CRC cells
A. Effects of the indicated PUFAs on the growth of 3D tumor spheroids generated from 5FU-R cells in the presence of 22 mM sodium bicarbonate. Indicated FAs were introduced starting from day three and replaced every three days.
B. Simplified schematic diagram of cell death pathways. The red font indicates the point of inhibition.
C. Western blot analysis of caspase 3 and cleaved caspase 3 levels in 5FU-R cells with indicated PUFAs (100 μM) for 24 h or etoposide (25 μM) for 6 h. β-actin served as an internal reference.
D, E. Cell survival of 5FU-R cells treated with a gradient concentration of PUFAs and **(D)** 20 μM necrostatin-1, **(E)** 10 μM ferrostatin-1, or 10 μM liproxstatin-1 for 24 h
F, G. (F) Representative images of cleaved caspase 3 and 4-HNE IHC staining of WT and 5FU-R HCT8 xenograft tumor sections with the indicated diets, scale bar = 100 μm. **(G)** AOD of cleaved caspase 3 and 4-HNE in the indicated xenograft tumors.
H, I. Levels of **(H)** MDA and **(I)** LPO in 5FU-R and corresponding WT cells were measured after treatment with 100 μM PUFAs for 24 h. The values were normalized with the total protein concentration.
J. Mitochondrial ultrastructures of 5FU-R and corresponding WT cells were observed after treatment with 100 μM PUFAs for 24 h, scale bar = 5 μm/1 μm
K. 5FU-R and corresponding WT cells were treated with 100 μM PUFAs for 24 h and then stained with JC-1 (2 μM) for 20 min. JC-1 aggregates (red) indicate a high ΔΨm, and JC-1 monomers (green) indicate a low ΔΨm, scale bar = 10 μm
L. 5FU-R and corresponding WT cells were treated with 100 μM PUFAs for 24 h and then stained with C11-BODIPY (5 μM) for 30 min. Oxidized C11-BODIPY (green) indicates mitochondrial lipid peroxidation, scale bar = 10 μm.
Data are shown as mean ± SD. The statistical analyses were performed using the unpaired Student's *t*-test or ANOVA. $^{*}P < 0.05$, $^{**}P < 0.01$, $^{***}P < 0.001$, or ns = not significant. SD, standard deviation; ANOVA, analysis of variance; CRC, colorectal cancer; 5FU-R, 5-fluorouracil-resistant; PUFA, polyunsaturated fatty acid; MDA, Malondialdehyde; LPO, lipid peroxidation; IHC, immunohistochemistry. (For interpretation of the references to color in this figure legend, the reader is referred to the Web version of this article.)

5-FU strongly suppressed the growth of 5FU-R 3D spheroids 6–9 days after exposure (Fig. 4C).

We further investigated the therapeutic potential of ferroptosis inducers for the treatment of 5FU-R CRC tumors in vivo. While administering RSL3 alone did not elicit any significant impact on the growth of $CDX^{HCT8\ WT}$ tumors in vivo, it effectively inhibited the growth of $CDX^{HCT8\ 5FU-R}$ tumors. Furthermore, the combination of RSL3 with 5-FU demonstrated synergistic anticancer effects on $CDX^{HCT8\ 5FU-R}$ tumors (Fig. 4D–F), which is consistent with our in vitro findings (Fig. 4C). In $CDX^{HCT8\ WT}$ tumors, treatment with RSL3 alone did not have any discernible impact on the staining of Ki67, cleaved caspase-3, or 4-HNE. However, it resulted in a significant reduction in the Ki67-positive rate and an increase in the staining intensity of 4-HNE in $CDX^{HCT8\ 5FU-R}$ tumors (Fig. 4G–J). Likewise, combined treatment with RSL3 and 5-FU further decreased the Ki67 positive rate and increased the staining intensity of 4-HNE in $CDX^{HCT8\ 5FU-R}$ tumors (Fig. 4G–J).

3.6. Dysfunction of the ferroptosis defense system in 5FU-R CRC cells

The fundamental regulatory mechanism of ferroptosis involves a dynamic interplay between "oxidative damage" and "antioxidant defense" [17]. These findings suggest that PUFAs or ferroptosis inducers trigger a cascade of LPO and subsequent oxidative damage in 5FU-R CRC cells. Furthermore, exploring whether the ferroptosis vulnerability of 5FU-R CRC cells is solely due to an overload of oxidative damage or a simultaneous deficiency in ferroptosis defense systems is imperative.

We further investigated the ferroptosis defense systems in 5FU-R CRC cells, which include the GPX4-GSH system [12], ferroptosis suppressor protein 1 (FSP1)- CoQH2 system [39,40], GTP cyclohydrolase 1 (GCH1)-tetrahydrobiopterin (BH4) system [41], and DHODH-CoQH2 system [18] (Fig. 5A). Initially, the GPX4-GSH system was identified as the principal defense mechanism against ferroptosis. 5FU-R CRC cells showed higher levels of total glutathione and a lower GSH/GSSG ratio than the corresponding WT cells. Nevertheless, brief exposure to DHA significantly augmented the total glutathione levels and reduced the GSH/GSSG ratio in WT CRC cells, whereas this response was considerably weaker in 5FU-R CRC cells (Fig. 5B). Compared to WT CRC cells, 5FU-R CRC cells showed elevated expression levels of solute carrier family 7 member 11 (SLC7A11) and GPX4; however, 5FU-R CRC cells displayed a reduced SLC7A11-GSH-GPX4 axis response to exogenous DHA (Fig. 5C and D). These findings indicate that the GPX4-GSH system in 5FU-R CRC cells experiencing overload may face challenges in effectively responding to further oxidative damage. Subsequently, the FSP1-CoQH2 system was identified, revealing that the expression levels of FSP1 were not significantly different between 5FU-R CRC cells and the corresponding WT cells, with both cell types demonstrating comparable upregulation in response to DHA treatment (Fig. 5C, **S6A**). Recent studies demonstrated the indispensability of FSP1 myristoylation for its antiferroptotic function [39]. The inhibition of myristoylation (IMP-1088) did not change significantly in cell death following RSL3 treatment in both 5FU-R and WT CRC cells (Fig. S6B). These results indicate that the FSP1-CoQH2 system was effective in both 5FU-R and WT cells, while its possible dependency on unknown mechanisms beyond myristoylation modification. In the GCH1-BH4 system, the expression of GCH1 was not significantly different between 5FU-R and WT CRC cells, and the levels of GCH1 did not display any response to exogenous DHA (Fig. 5C–S6C). Furthermore, the DHODH-CoQH2 system was recently identified as a novel ferroptosis defense mechanism within mitochondria [18]. DHODH expression was substantially increased in 5FU-R CRC cells compared to WT cells (Fig. 5C–E). Intriguingly, administration of DHA resulted in a marked elevation of DHODH levels in WT CRC cells but failed to induce a similar increase in 5FU-R CRC cells (Fig. 5C–E). Although brequinar, a DHODH inhibitor, significantly increased the susceptibility of WT CRC cells to ferroptosis triggered by RSL3, it did not exacerbate RSL3-induced ferroptosis in 5FU-R CRC cells (Fig. 5F). Overall, our results suggest that despite the elevated expression of DHODH in 5FU-R CRC cells, the DHODH-CoQH2 system displays a deficiency in ferroptosis defense.

3.7. DHODH- and Gpx4-deficient mitochondria induce ferroptosis vulnerability

Recent studies suggest that cancer cells with low GPX4 expression rely on DHODH or FSP1 for ferroptosis protection [18,39,40], while those with low DHODH, FSP1, or GCH1 expression are more susceptible to GPX4 inhibitors [17]. However, our results contradict this hypothesis by demonstrating that high GPX4 and DHODH levels do not effectively defend against DHA-induced peroxidation in 5FU-R CRC cells. As DHODH is a mitochondria-localized ferroptosis defense system, and cytosolic and mitochondrial GPX4 defends against ferroptosis within distinct subcellular compartments [18], the defense inadequacy of the mitochondrial subcellular compartment may induce ferroptosis vulnerability in 5FU-R CRC cells. To test this possibility, we investigated the mitochondrial content and function in 5FU-R CRC cells, revealing a reduced mitochondrial content (Fig. 5G) and downregulation of mitochondrial respiratory chain enzymes (Fig. 5H and I) compared with those of WT cells. Considering that impaired mitochondria serve as the primary origin of excessive ROS within the cell [42], including species such as the superoxide radical ($O_2^{\cdot-}$), hydrogen peroxide (H_2O_2), and the hydroxyl radical (OH·) (Fig. S6D), we determined the levels of total ROS

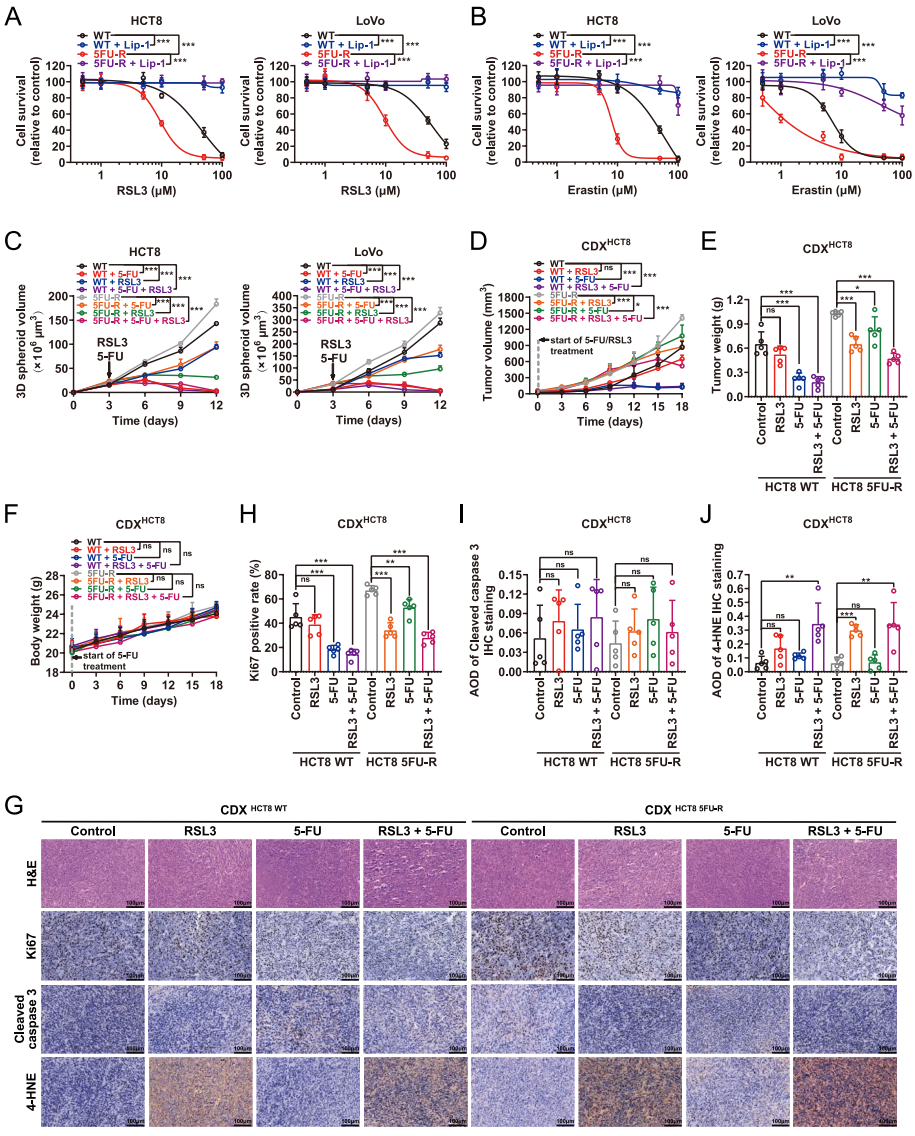

Fig. 4. 5FU-R CRC cells are sensitive to ferroptosis inducers

A, B. Cell viability in 5FU-R and corresponding WT cells treated with different doses of **(A)** RSL3 for 4 h or **(B)** erastin for 12 h, following pretreatment with liproxstatin-1 (10 μM) for 24 h

C. Effects of 5-FU (10 μM) and RSL3 (1 μM) on the growth of 3D tumor spheroids generated from 5FU-R cells and their WT counterparts. 5-FU or RSL3 were introduced starting from day three and replaced every three days.

D. Tumor volumes of WT and 5FU-R HCT8 xenografts with 5-FU (25 mg kg^{-1}, 3 times a week, intraperitoneally) or RSL3 (100 mg kg^{-1}, 2 times a week, intratumorally) treatment at different time points (days).

E. Tumor weights of WT and 5FU-R HCT8 xenografts with 5-FU or RSL3 treatment.

F. Weights of mice for WT and 5FU-R HCT8 xenografts with different treatments at different time points (days).

G–J. (G) Representative images of H&E staining, Ki67, cleaved caspase 3, and 4-HNE IHC staining on WT and 5FU-R HCT8 xenograft tumor sections with the indicated treatment, scale bar = 100 μm. AOD of **(H)** Ki67, **(I)** cleaved caspase 3, and **(J)** 4-HNE in the indicated xenograft tumors.

Data are shown as mean ± SD. The number of mice in each group was five. The statistical analyses were performed using the unpaired Student's t-test or ANOVA. $*P < 0.05$, $**P < 0.01$, $***P < 0.001$, or ns = not significant. SD, standard deviation; ANOVA, analysis of variance; CRC, colorectal cancer; 5FU-R, 5-fluorouracil-resistant.

and specific ROS species. Total ROS levels and those of all three ROS species displayed a remarkable increase in 5FU-R CRC cells (Figs. S6E–H). Collectively, these findings suggested that mitochondrial damage accompanies 5-FU resistance in CRC cells.

To ascertain whether mitochondrial impairment is linked to inadequate ferroptosis protection in 5FU-R CRC cells, we isolated cytosolic and mitochondrial fractions. DHA stimulation in WT CRC cells significantly increased GPX4 contents in the cytosol ($GPX4^{Cyto}$) and mitochondria ($GPX4^{Mito}$). However, $GPX4^{Cyto}$ did not exhibit a response to DHA, and $GPX4^{Mito}$ contents exhibited a further reduction in 5FU-R CRC cells (Fig. 5J). DHODH was predominantly expressed in the mitochondria as opposed to in the cytosol, and the mitochondrial DHODH ($DHODH^{Mito}$) level was significantly elevated in response to exogenous DHA. Interestingly, DHODH was abundantly expressed in the cytosol of 5FU-R CRC cells as opposed to the mitochondria, and $DHODH^{Mito}$ contents decreased even further in response to DHA (Fig. 5J). Colocalization studies confirmed these findings (Fig. 5K–S6I). These data suggest that $GPX4^{Mito}$ and $DHODH^{Mito}$ in 5FU-R CRC cells appear inadequate for defending against ferroptosis, exacerbated lipid peroxide accumulation, and mitochondrial ferroptosis defense impairments.

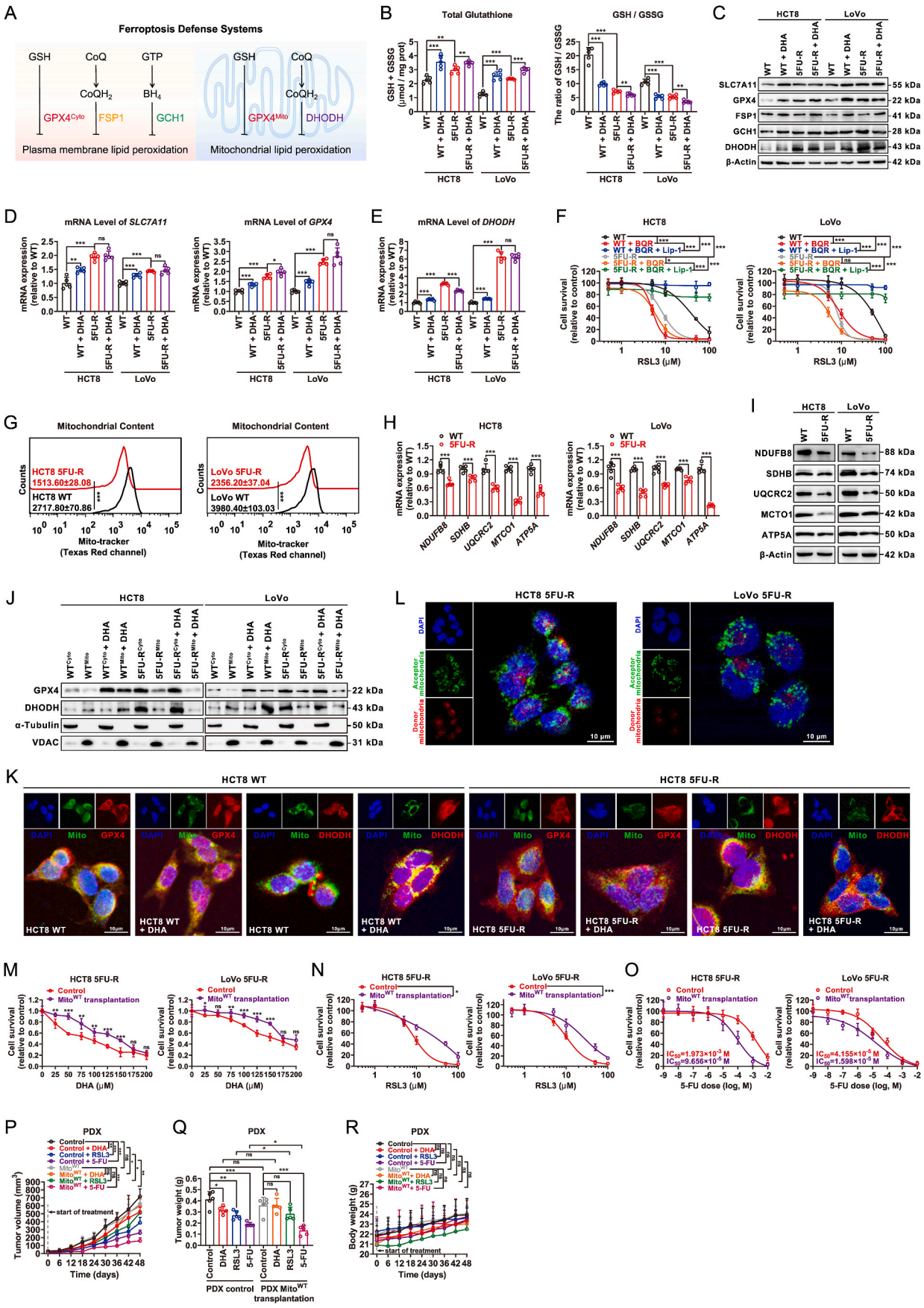

(caption on next page)

Fig. 5. Mitochondrial ferroptosis defense systems in 5FU-R CRC cells
A. Simplified schematic diagram of ferroptosis defense mechanisms.
B. The total glutathione level and the ratio of reduced/oxidized glutathione were measured in 5FU-R and corresponding WT cells upon treatment with DHA (100 μM) for 24 h
C. Western blot analysis of SLC7A11, GPX4, FSP1, GCH1, and DHODH levels in 5FU-R and corresponding WT cells upon treatment with DHA (100 μM) for 24 h. β-actin served as an internal reference.
D. mRNA levels of *SLC7A11* and *GPX4* in the indicated cancer cells. *ATCB* served as an internal reference.
E. mRNA level of *DHODH* in the indicated cancer cells. *ATCB* served as an internal reference.
F. Cell viability in 5FU-R and corresponding WT cells treated with different doses of erastin and co-treated with brequinar (500 μM) for 4 h, following pretreatment with liproxstatin-1 (10 μM) for 24 h
G. Flow cytometric histogram of the fluorescence intensity (Texas red channel) in 5FU-R and corresponding WT cells upon staining with MitoTracker Red (50 nM) for 30 min.
H, I. (H) mRNA levels of *NDUFB8*, *SDHB*, *UQCRC2*, *MCTO1*, or *ATP4A* (bar charts) and **(I)** their protein expression (immunoblots) in the indicated cancer cells. *ATCB*/β-actin served as an internal reference.
J. Western blot analysis of cytosolic and mitochondrial GPX4 or DHODH proteins from 5FU-R and corresponding WT cells, following treatment with 100 μM DHA for 24 h. α-tubulin and VDAC served as the cytosolic and mitochondrial internal reference, respectively.
K. Confocal microscopy images of co-localization of GPX4 or DHODH on the mitochondria in 5FU-R and corresponding WT cells, following treatment with 100 μM DHA for 24 h. The images were collected with the same exposure time for all specimens. DAPI (blue), mitochondria (green), GPX4 or DHODH (red). Scale bar = 10 μm
L. Confocal microscopy images of "donor" mitochondria (red) transplanted into the "acceptor" cells (green), scale bar = 10 μm.
M-O. Cell survival in mitochondria transplanted 5FU-R cells and control cells treated with a gradient in the concentration of **(M)** DHA for 24 h, **(N)** RSL3 for 4 h, or **(O)** 5-FU for 72 h
P. Tumor volumes of mitochondria transplanted and control PDXs with a DHA-rich diet, RSL3 (100 mg kg^{-1}, 2 times a week, intratumorally), or 5-FU (25 mg kg^{-1}, 3 times a week, intraperitoneally) treatment at different time points (days).
Q. Tumor weights of PDXs with the indicated diets and 5-FU treatment.
R. Weights of mice for PDXs with different treatments at different time points (days).
Data are shown as mean ± SD. The number of mice in each group was five. The statistical analyses were performed using the unpaired Student's *t*-test or ANOVA. $*P < 0.05$, $**P < 0.01$, $***P < 0.001$, or ns = not significant. SD, standard deviation; ANOVA, analysis of variance; CRC, colorectal cancer; 5FU-R, 5-fluorouracil-resistant; DHA, docosahexaenoic acid; PDX, patient-derived xenograft. (For interpretation of the references to color in this figure legend, the reader is referred to the Web version of this article.)

To confirm the impact of mitochondrial abnormalities on ferroptosis vulnerability and 5-FU sensitivity in CRC, next, we performed in vitro and in vivo mitochondrial transplantation. Transplanting mitochondria from WT CRC cells into 5FU-R CRC cells (Fig. 5L) increased the survival of cells when exposed to DHA below 150 μM (Fig. 5M) and partially abolished RSL3-induced ferroptosis and 5-FU resistance (Fig. 5N and O). In vivo mitochondrial transplantation into PDX^{5FU-R} tumors produced similar but weak results (Fig. 5P–R). Collectively, these data indicate that restoring mitochondrial function partially alleviates ferroptosis vulnerability and 5-FU resistance in 5FU-R CRC.

3.8. *DHODH is a potential anti-cancer target in 5FU-R CRC*

The knockdown of *DHODH* in WT CRC cells (Fig. 6A) significantly increased DHA and RSL3 cytotoxicity, whereas the corresponding effect in 5FU-R CRC cells was negligible (Fig. 6B and C). This result implies that DHODH in 5FU-R CRC cells lacks effective ferroptosis defense. DHODH is a dehydrogenase that is a promising target for broad-spectrum cancer therapy due to its rate-limiting role in de novo pyrimidine synthesis in the "mitochondrial" step (Fig. 6D) [21,22,43]. Because we found that DHODH was highly expressed in 5FU-R CRC cells and primarily localized in the cytosol (Fig. 5J, K, S6I), we evaluated the effects of *DHODH* knockdown on CRC cells. Knockdown of *DHODH* resulted in a significant reduction in the invasion, proliferation, and migration capabilities in both 5FU-R and the corresponding WT CRC cells, with a more pronounced effect observed in the former (Fig. 6E–G). Furthermore, *DHODH* knockdown increased 5-FU sensitivity in 5FU-R CRC cells but had no significant effect on WT cells (Fig. 6H). Our data therefore support the idea that extramitochondrial DHODH plays a role in facilitating malignant biological behaviors in cancer cells and suggest that DHODH is a promising therapeutic target for 5FU-R CRC.

We further explored the therapeutic potential of DHODH inhibition in vivo. *DHODH* knockdown effectively inhibited the growth of $CDX^{HCT8\ WT}$ and $CDX^{HCT8\ 5FU-R}$ tumors in mice, particularly in the latter (Fig. 6I, **S7A, B**). Although *DHODH* knockdown did not further suppress 5-FU-treated $CDX^{HCT8\ WT}$ tumors, it significantly restored 5-FU sensitivity to $CDX^{HCT8\ 5FU-R}$ tumors (Fig. 6I–S7A, B). *DHODH* knockdown significantly reduced Ki67 staining in $CDX^{HCT8\ 5FU-R}$ tumors but not in $CDX^{HCT8\ WT}$ tumors and increased 4-HNE staining in $CDX^{HCT8\ WT}$ but not in $CDX^{HCT8\ 5FU-R}$ tumors (Figure S7C, SJ, K). Combining *DHODH* knockdown and 5-FU treatment synergistically suppressed Ki67 staining in $CDX^{HCT8\ 5FU-R}$ tumors, but had no impact on 4-HNE staining (Figure S7C, SJ, K). These data indicate independent roles of DHODH-mediated ferroptosis defense and malignant behaviors in 5FU-R CRC. We also investigated the therapeutic potential of DHODH inhibitors in the treatment of PDX^{5FU-R} tumors in vivo using teriflunomide, an FDA-approved drug with DHODH activity. Teriflunomide suppressed PDX^{5FU-R} tumor growth (Fig. 6L and M). Notably, combined teriflunomide and 5-FU administration nearly completely inhibited PDX^{5FU-R} tumor growth, whereas individual administration of either agent was less effective (Fig. 6L and M). Importantly, DHODH inhibition had no significant impact on animal weight, indicating that the treatment was well tolerated in vivo (Fig. S7D). While the no-response group exhibited elevated DHODH expression (Fig. 6N and O), DHODH levels did not correlate with poor prognosis in patients with CRC who received preoperative fluorouracil analog-based chemotherapy (Fig. 6P). Overall, DHODH appears to be a promising target for inhibiting tumor growth and reversing 5-FU resistance in 5FU-R CRC.

3.9. *Extramitochondrial DHODH is involved in pyrimidine biosynthesis in 5FU-R CRC*

DHODH is mainly located in the inner mitochondrial membrane, where it facilitates the conversion of dihydroorotate (DHO) to orotate within the de novo pyrimidine synthesis pathway [20]. However, our previous results showed a substantial presence of DHODH in the cytoplasm of 5FU-R CRC cells. To explore this further, we investigated the factors contributing to DHODH redistribution. Prior research has demonstrated that importing DHODH into mitochondria requires an N-terminal segment (Fig. 7A) and an inner membrane potential [32]. The results of N-terminal sequencing indicated that there was no discernible distinction between $DHODH^{Mito}$ and $DHODH^{Cyto}$ in the N-terminal regions of 5FU-R CRC cells (Fig. 7B). $DHODH^{Mito}$, $DHODH^{Cyto}$, and endogenous human DHODH (used as a positive control), but

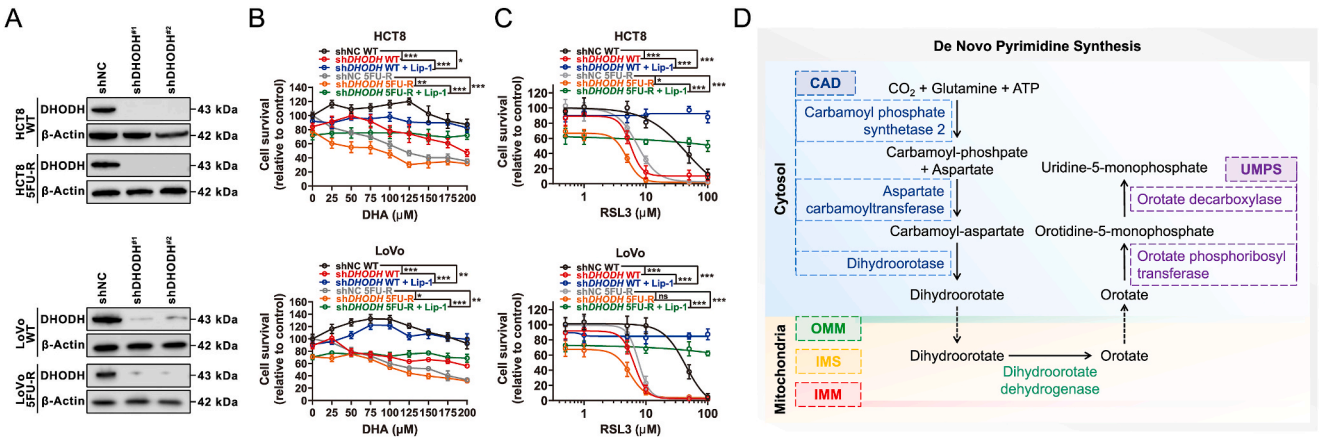

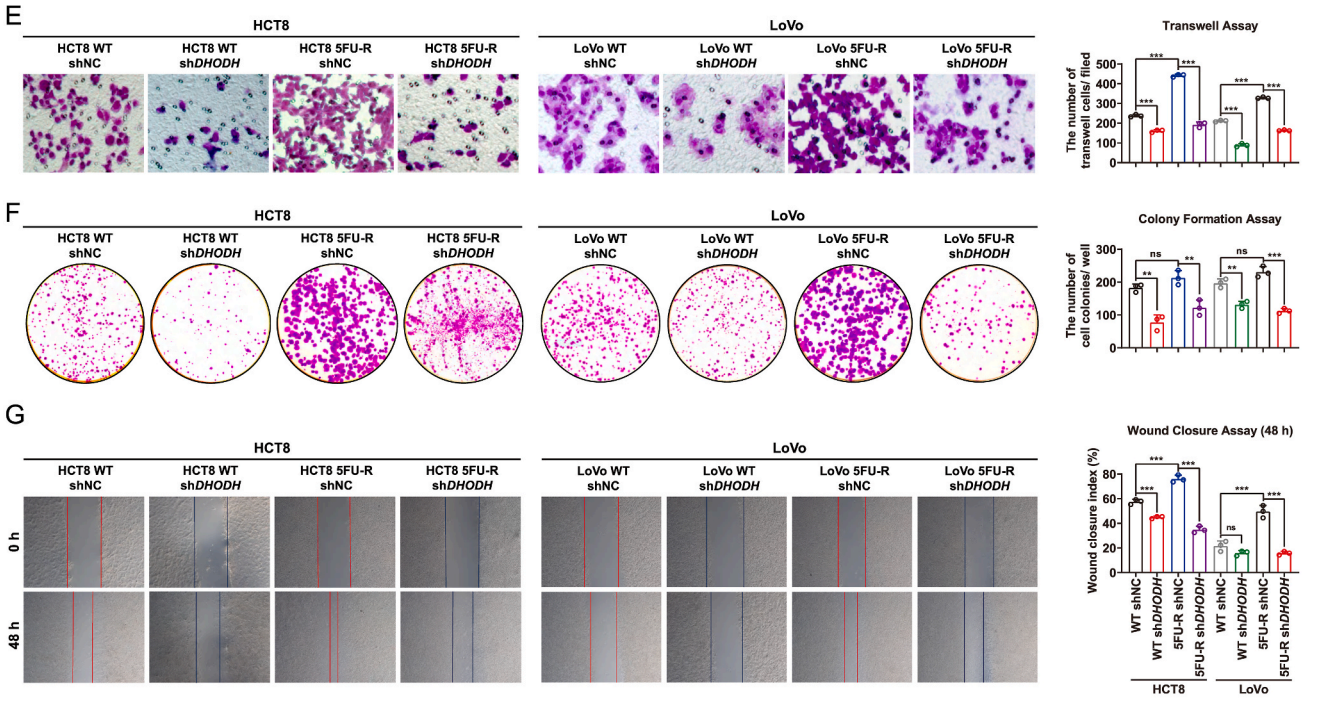

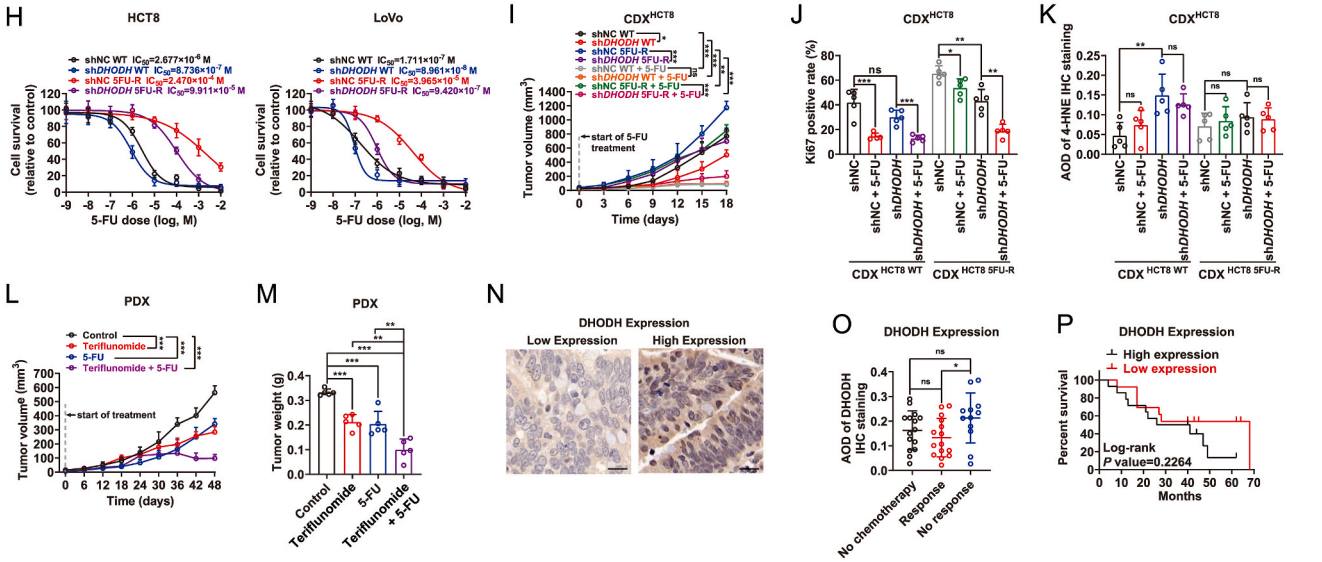

(caption on next page)

Fig. 6. DHODH as a potential anti-cancer target in 5FU-R CRC
A. DHODH protein levels in negative control (shNC) and *DHODH* knockdown (sh*DHODH*) CRC cells. β-actin served as an internal reference.
B, C. Cell survival in 5FU-R and corresponding WT cells with indicated genotypes treated with different doses of **(B)** DHA for 24 h or **(C)** RSL3 for 4 h, following pretreatment with liproxstatin-1 (10 μM) for 24 h.
D. Simplified schematic diagram of de novo pyrimidine synthesis.
E–G. (E) Transwell invasion, **(F)** colony formation, and **(G)** wound healing assays in 5FU-R and corresponding WT cells with the indicated genotypes.
H. Cell survival in 5FU-R and corresponding WT cells with indicated genotypes treated with different doses of 5-FU for 72 h.
I. Tumor volumes of WT and 5FU-R HCT8 xenografts with indicated genotypes treated with 5-FU (25 mg kg^{-1}, 3 times a week, intraperitoneally) at different time points (days).
J, K. (J) Ki67 positive rates and **(K)** AOD of 4-HNE in the indicated xenograft tumors.
L. Tumor volumes of PDXs with teriflunomide (10 mg kg^{-1} in 0.5 % methyl cellulose solution, per day, intragastrically) or 5-FU (25 mg kg^{-1}, 3 times a week, intraperitoneally) treatment at different time points (days).
M. Tumor weights of PDXs with teriflunomide or 5-FU treatment.
N. Representative images of IHC staining for DHODH on tumor sections in CRC patients, scale bar = 50 μm.
O. Comparison of IHC staining (AOD) for DHODH in three CRC subcohorts.
P. Kaplan–Meier survival curves of disease-free survival of CRC patients on fluorouracil analog-based chemotherapy with high (AOD ≥0.17, n = 14) or low (AOD <0.17, n = 13) DHODH expression as assessed by the IHC images.
Data are shown as means ± SD. The number of mice in each group was five. The statistical analyses were performed using the unpaired Student's *t*-test or ANOVA, and survival was compared by log rank (Mantel–Cox) testing. $^{*}P < 0.05$, $^{**}P < 0.01$, $^{***}P < 0.001$, or ns = not significant. SD, standard deviation; ANOVA, analysis of variance; CRC, colorectal cancer; 5FU-R, 5-fluorouracil-resistant; IHC, immunohistochemistry; DHA, docosahexaenoic acid; PDX, patient-derived xenograft.

not Δ29DHODH (N-terminally truncated DHODH) (Fig. 7A), could be imported into the inner mitochondrial membrane of yeast mitochondria (Fig. 7C). These findings indicate that the extramitochondrial DHODH present in 5FU-R CRC cells possesses both the structural and functional characteristics necessary for its localization within the mitochondrial inner membrane. Furthermore, to determine the ATP requirement for DHODH localization, we conducted a $DHODH^{Cyto}$ import reaction with ATP depletion using oligomycin and carboxyatractyloside. The import of DHODH into mitochondria was reduced in ATP-depleted mitochondria (Fig. 7D). Additionally, the mitochondrial uncoupler protonophore (ionophore uncoupler trifluorocarbonylcyanide phenylhydrazone; FCCP, Agilent Technologies) significantly reduced DHODH import (Fig. 7E). These results imply that DHODH import into mitochondria relies on ATP and maintaining the mitochondrial membrane potential. Therefore, the translocation of DHODH into the cytosol in 5FU-R CRC cells likely results from mitochondrial dysfunction rather than DHODH abnormalities.

The core catalytic domain of DHODH is highly conserved across species, with infrequent mutations [31]. Our previous analysis suggests that cytosolic DHODH likely retains its catalytic function in 5FU-R CRC cells. To evaluate the DHODH activity, we incorporated $DHODH^{Mito}$, $DHODH^{Cyto}$, and endogenous human DHODH (used as a positive control) into a DHO-containing reaction system. $DHODH^{Mito}$ in the reaction system exhibited DHO catalytic activity, which was consistent with the activity of the positive control (Fig. 7F). Together, our data support the conclusion that extramitochondrial DHODH plays a role in pyrimidine biosynthesis in 5FU-R CRC, akin to mitochondrial DHODH.

3.10. Increased pyrimidine synthesis contributes to 5-FU resistance in 5FU-R CRC cells

Next, we sought to elucidate the mechanism underlying the regulatory role of DHODH in tumor growth and its impact on the 5-FU treatment response in CRC. We compared intracellular levels of 5-FU and its bioactive product, FdUMP, in WT and 5-FU-R CRC cells after 5-FU exposure. Notably, no significant difference in the intracellular levels of 5-FU and FdUMP between 5FU-R CRC and WT cells was found (Fig. 8A–S8A). This observation suggests that the uptake and intracellular metabolism of 5-FU are not primary determinants of 5-FU resistance in CRC cells. The primary mechanism of the anticancer activity of 5-FU involves inhibiting thymidylate synthase (TS) through FdUMP [44] (Fig. 8B). We identified metabolites and key enzymes involved in the de novo pyrimidine and deoxythymidine monophosphate (dTMP) synthesis pathways. Intermediates in these pathways and dTMP synthesis were significantly elevated in 5FU-R cells compared to those in WT cells (Fig. 8C). The expression levels of genes involved in nucleotide metabolism were generally higher in 5FU-R cells than in WT cells (Fig. 8D). Similarly, protein expression of carbamoyl phosphate synthetase 2-aspartate carbamoyltransferase-dihydroorotase (CAD) and TS was elevated in 5FU-R cells compared to that in WT cells (Fig. 8E). Further, the no-response group of the CRC patient cohort exhibited elevated levels of uridine monophosphate (UMP), deoxyuridine monophosphate (dUMP), and dTMP compared to the response group (Fig. 8F–H, S8A). Specifically, significantly increased dUMP levels were observed in primary tumors of patients who received preoperative fluorouracil analog-based chemotherapy and had poor disease-free survival (Fig. 8I–S8B). High DHODH expression increases the metabolic flux of de novo pyrimidine synthesis. The knockdown of *DHODH* in 5FU-R CRC cells led to a reduction in CAD and TS expression (Fig. 8J). Moreover, UMP, dUMP, and dTMP levels decreased in 5FU-R CRC cells after *DHODH* knockdown (Fig. 8K–M). In summary, our data suggest a novel mechanism of 5-FU resistance in which CRC cells accumulate intracellular pyrimidine pools, rendering 5-FU ineffective through molecular competition. Importantly, inhibiting DHODH to regulate pyrimidine metabolism significantly enhances chemosensitivity (see Fig. 9).

4. Discussion

Chemoresistance is the leading cause of treatment failure in CRC, with 5-FU being the primary chemotherapy agent employed. Numerous mechanisms are thought to underlie 5-FU resistance [3,45]. While previous studies have predominantly focused on chemoresistance arising from altered drug transport [46], our study provides compelling evidence that 5-FU resistance can be countered in CRC by targeting DHODH-related ferroptosis and pyrimidine biosynthesis. Specifically, we elucidated the mechanism underlying 5-FU resistance in CRC cells, whereby the cytosolic DHODH-mediated pathway enhanced intracellular pyrimidine pools, reducing 5-FU metabolite concentrations. Based on these findings and previous research, we identified a novel metabolic mechanism that renders CRC cells vulnerable to ferroptosis, driven by lipid metabolism reprogramming and mitochondrial DHODH deficiency. Thus, utilizing ferroptosis sensitivity or targeting DHODH may contribute to novel therapeutic strategies for advanced CRC with first-line treatment failure.

Lipid metabolic reprogramming has recently been identified as a cancer hallmark [34,35]. Several lipid metabolism inhibitors have demonstrated promising anticancer effects in preclinical studies and clinical trials [47,48]. However, the role of lipid metabolic reprogramming in chemoresistance remains unclear. Our study comprehensively examined lipid metabolism reprogramming in 5FU-R CRC cells and demonstrated that these cells accumulated excessive lipids owing to

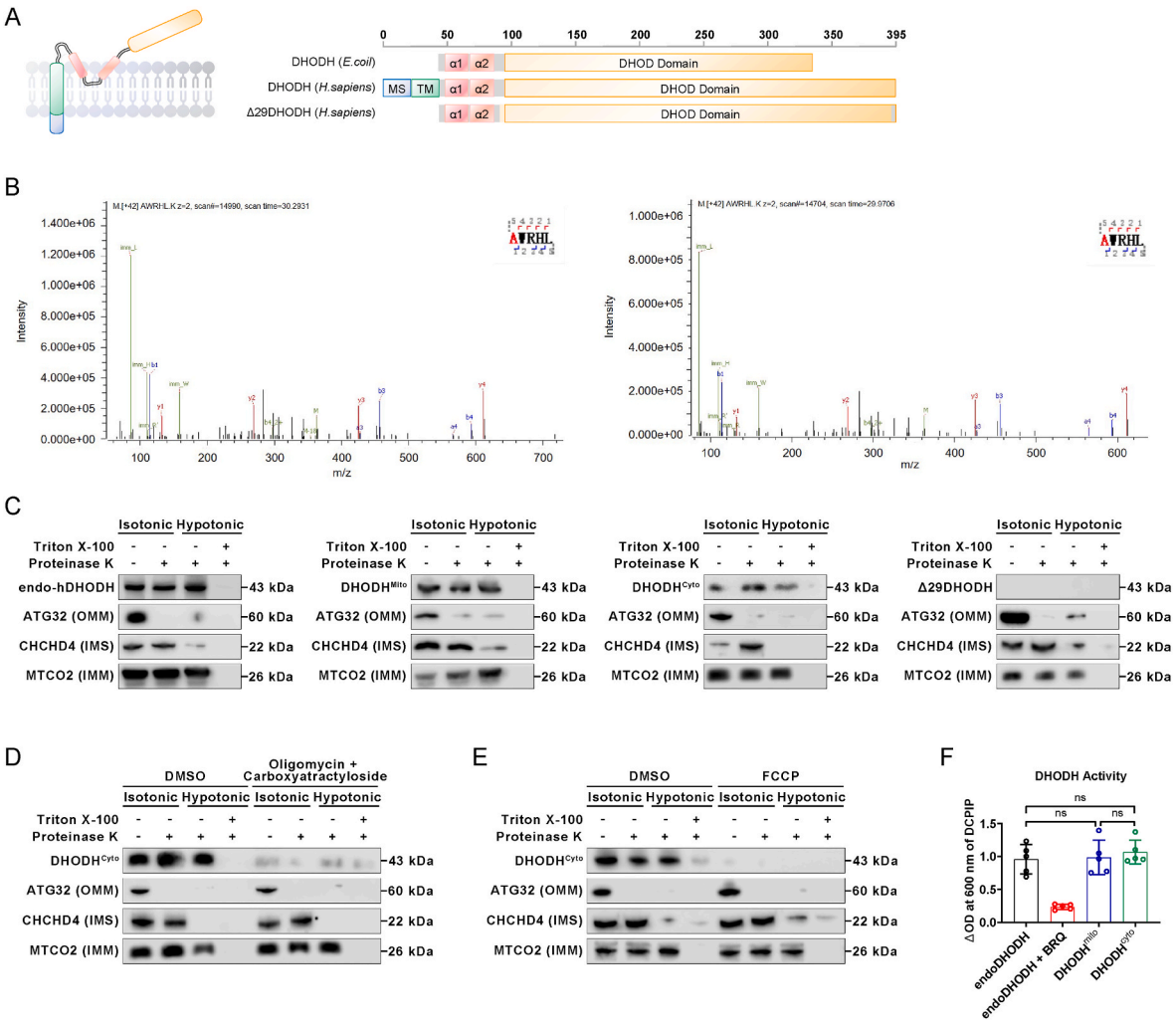

Fig. 7. Mitochondrial DHODH is normal in both structure and function.

A. Simplified schematic diagram of N-terminal sequences of DHODH proteins. The N-terminus of DHDOH (*H. sapiens*) contains a mitochondrial signal (MS) and a transmembrane segment (TM).

B. N-terminal sequence analysis of $DHODH^{Mito}$ (left) and $DHODH^{Cyto}$ (right).

C. The DHODH proteins were imported into yeast mitochondria, followed by subjecting the mitochondria to proteinase K digestion in either isotonic or hypotonic buffer. Western blot analysis of DHODH was performed. ATG32, CHCHD4, and MTCO2 served as the controls for the outer mitochondrial membrane (OMM), intermembrane space (IMS), and inner mitochondrial membrane (IMM), respectively.

D, E. Yeast mitochondria were treated with **(D)** oligomycin (10 μM) and carboxyatractyloside (20 μM), or **(E)** FCCP (5 μM); then, the mitochondria were incubated with the indicated DHODH proteins. Effects of inhibitors on the import of DHODH into yeast mitochondria were detected.

F. DHODH activity of cytosolic and mitochondrial DHODH.

Data are shown as mean ± SD. The statistical analyses were performed using the ANOVA. ns = not significant. FCCP, ionophore uncoupler trifluorocarbonylcyanide phenylhydrazone; SD, standard deviation; ANOVA, analysis of variance.

imbalances in fatty acid uptake, synthesis, and oxidation. Among various fatty acids, PUFAs are notable for their tendency to accumulate and exert cytotoxic effects on 5FU-R CRC cells. We found a positive correlation between the number of double bonds in PUFAs and their accumulation capability and anticancer effects. These findings suggest that the intrinsic chemical properties of PUFAs directly induce LPO in 5FU-R CRC cells. This observation is in line with the results of previous research indicating that owing to numerous double bonds, PUFAs are primary substrates for LPO [16]. Moreover, our results are consistent with those of previous studies [19], which demonstrated that 5-FU resistance in CRC cells is linked to irreversible impairment of mitochondria and elevated ROS production. Notably, 5FU-R CRC cells encountered excessive LPO due to abnormal lipid metabolism and impaired mitochondrial function. Our results confirmed that exogenous PUFAs act similarly to ferroptosis inducers, eliciting cytotoxicity in 5FU-R CRC cells. Importantly, our investigation revealed that these cells are more susceptible to ferroptosis owing to aberrant metabolism. This observation is in line with the findings of previous research showing that various metabolic reactions can generate LPO products, emphasizing that metabolism is the primary driver of ferroptosis [14,49,50].

Extensive research has been conducted on the key factors that drive ferroptosis, including PUFA peroxidation, iron metabolism, and mitochondrial function [17,51]. However, despite rapid development in the past three years, the investigation of ferroptosis defense mechanisms remains in its nascent stages. The GPX4-GSH system is a well-studied ferroptosis defense mechanism. GPX4 comprises three isoforms with unique subcellular localizations: cytosolic, mitochondrial, and nuclear [17]. Prior to recent findings, it was commonly believed that only the cytosolic GPX4 isoform plays a role in defending against ferroptosis [52]; however, current research, including our study, indicates that both cytosolic and mitochondrial GPX4 defend against ferroptosis [18]. Our work demonstrates that mitochondrial GPX faces challenges in

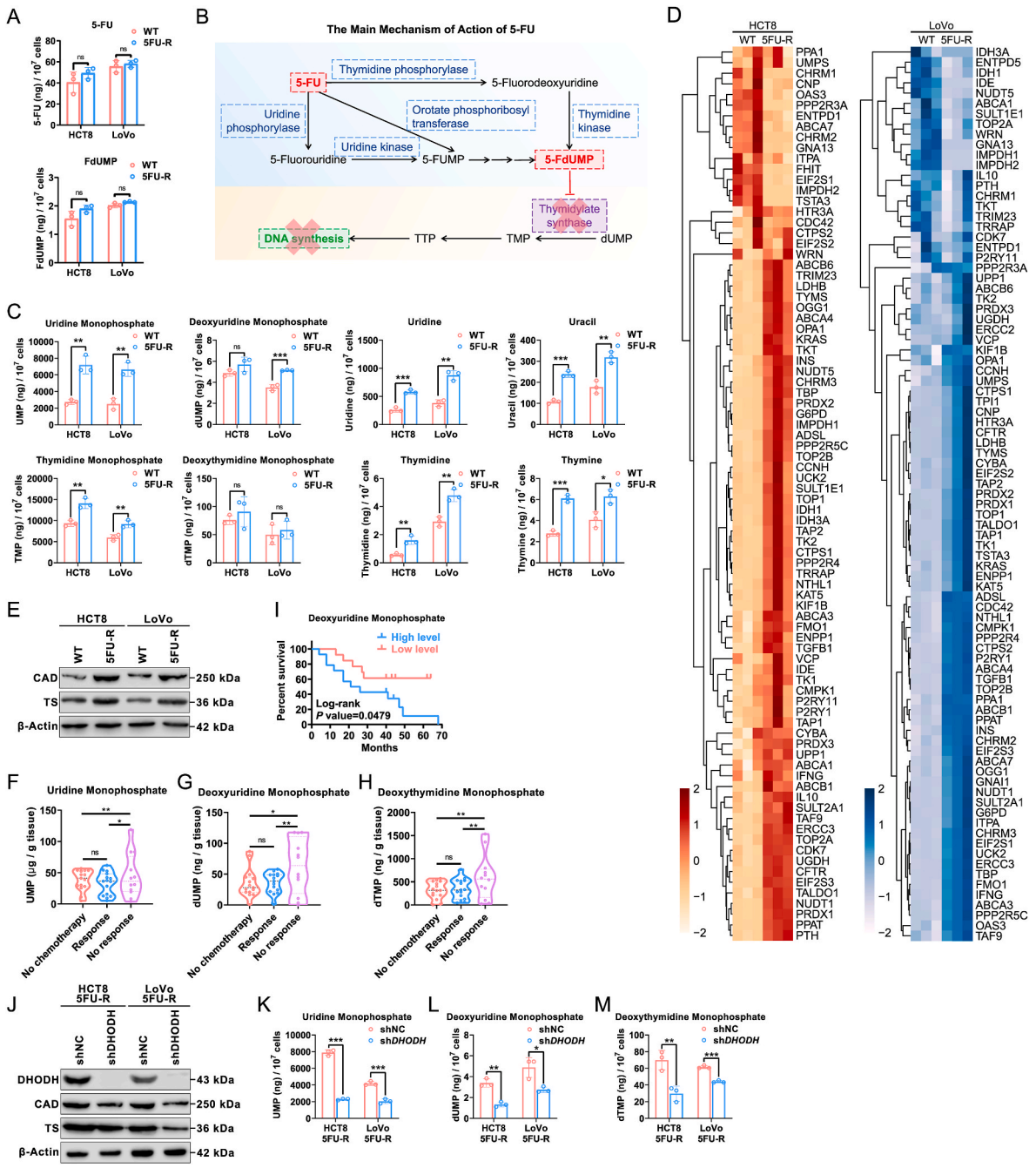

Fig. 8. Increased pyrimidine synthesis contributes to 5-FU resistance.

A. Intracellular concentrations of 5-FU and FdUMP were measured in 5FU-R and corresponding WT cells upon treatment with 5-FU (10 μM) for 12 h

B. Simplified schematic diagram: 5-FU suppresses pyrimidine synthesis by inhibiting TS.

C. Comparison of pyrimidine nucleotides and related substances in 5FU-R and corresponding WT cells.

D. PCR array of nucleotide metabolism gene expression in 5FU-R and corresponding WT cells. *ATCB* served as an internal reference.

E. Western blot analysis of CAD and TS levels in 5FU-R and corresponding WT cells. β-actin served as an internal reference.

F–H. Comparison of **(F)** UMP, **(G)** dUMP, and **(H)** dTMP levels in three CRC subcohorts.

I. Kaplan–Meier survival curves of disease-free survival of CRC patients on fluorouracil analog-based chemotherapy with high or low dUMP levels as assessed by HPLC.

J. Western blot analysis of CAD and TS levels in 5FU-R and corresponding WT cells with indicated *DHODH* genotypes. β-actin served as an internal reference.

K–M. Comparison of **(K)** UMP, **(L)** dUMP, and **(M)** dTMP levels in 5FU-R and corresponding WT cells with indicated *DHODH* genotypes.

Data are shown as mean ± SD. The statistical analyses were performed using the unpaired Student's *t*-test or ANOVA, and survival was compared by log rank (Mantel–Cox) testing. $^{*}P < 0.05$, $^{**}P < 0.01$, $^{***}P < 0.001$, or ns = not significant. SD, standard deviation; ANOVA, analysis of variance; CRC, colorectal cancer; 5FU-R, 5-fluorouracil-resistant; UMP, uridine monophosphate; dUMP, deoxyuridine monophosphate; CAD, carbamoyl phosphate synthetase 2-aspartate carbamoyltransferase-dihydroorotase; dTMP, deoxythymidine monophosphate; TS, thymidylate synthase.

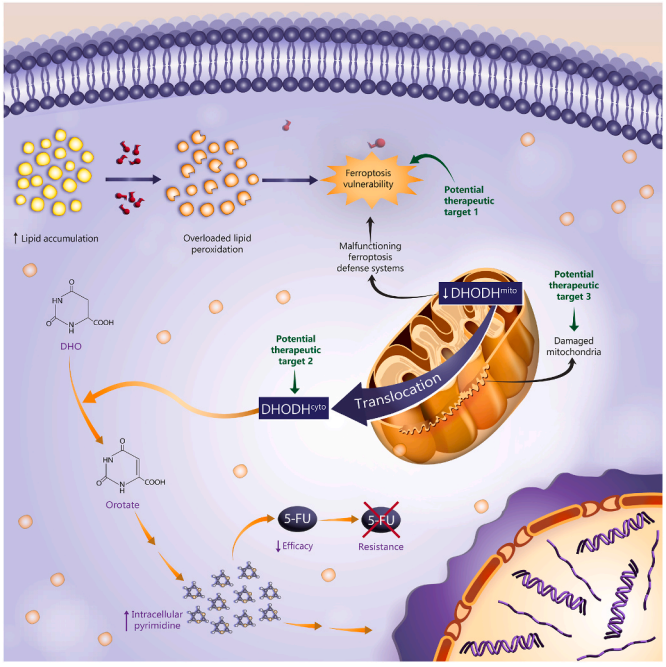

Fig. 9. Schematic of the proposed mechanism of DHODH in 5-FU-resistant CRC.

effectively countering PUFAs or ferroptosis inducers in 5FU-R CRC cells due to mitochondrial damage and oxidative stress. A recent study reported that mitochondrial DHODH compensates for GPX4 loss to detoxify mitochondrial LPO [18]. However, our findings indicate that, in the context of mitochondrial destruction, mitochondrial DHODH is ineffective in defending against ferroptosis in 5-FU-resistant states. Deactivating both mitochondrial GPX4 and DHODH poses a considerable challenge in mitigating potent mitochondrial LPO in 5FU-R CRC cells, ultimately inducing robust ferroptosis. Importantly, FSP1 and GCH1 were ineffective at inhibiting LPO in 5FU-R CRC cells subjected to PUFA treatment. This may be attributed to their absence from the mitochondria, rendering them incapable of detoxifying the lipid peroxides accumulating within this organelle. Thus, our results highlight the significance of subcellular compartmentalization in ferroptosis defense.

DHODH is primarily located in the inner mitochondrial membrane and drives intracellular pyrimidine biosynthesis [20]. Its well-established tumorigenic function has prompted extensive research on DHODH inhibitors for cancer therapy [22,23]. An unexpected finding from these studies is that DHODH levels are reduced within the mitochondria of 5FU-R CRC cells compared with those in the corresponding WT cells. This observation suggests the existence of cytosolic DHODH. The causes of this distribution shift and the role of cytosolic DHODH in malignancy and cancer chemoresistance remain elusive. Our study addressed these issues and demonstrated that the redistribution of DHODH in 5FU-R CRC cells was attributable to mitochondrial dysfunction rather than abnormalities in DHODH. Our key findings are as follows: (1) extramitochondrial DHODH from chemoresistant cells can enter the inner mitochondrial membrane of yeast; (2) no structural difference was noticed between cytosolic and mitochondrial DHODH in the N-terminal region, which determines mitochondrial localization; and (3) successful DHODH import into the mitochondria requires ATP supplementation and maintenance of the mitochondrial membrane potential. In addition, we found that cytosolic DHODH, like its mitochondrial counterpart, exhibited DHO catalytic activity and participated in pyrimidine biosynthesis in 5FU-R CRC cells. Enhanced pyrimidine synthesis in 5FU-R CRC cells expanded pyrimidine pools, competitively inhibiting 5-FU activity and ultimately promoting 5-FU resistance. Despite the ability of 5FU-R CRC cells to take up 5-FU from the extracellular milieu, they maintain a high pyrimidine/5-FU ratio, thereby sustaining chemoresistance. These results have led us to propose a novel cell-intrinsic mechanism for chemoresistance to pyrimidine analog chemotherapy, centered on pyrimidine metabolism reprogramming.

What do our findings mean for cancer therapy? **First, we identified the role of ferroptosis in chemoresistant CRC therapy.** Ferroptosis is gradually gaining importance in cancer treatment, with key signaling pathways such as those including PI3K [53], p53 [54], and BRCA1-associated protein 1 (BAP1) [55] regulating it. Certain cancer cells rely heavily on ferroptosis defense mechanisms under metabolic and oxidative stress conditions [15,56,57], making their disruption fatal. We found that intracellular PUFA accumulation, a high ROS load, and impaired mitochondrial DHODH defense systems render 5FU-R CRC cells susceptible to ferroptosis. These findings underscore the potential of a DHA-rich diet and pharmacological ferroptosis inducers such as RSL3 and erastin to inhibit CRC tumor growth and partially reverse 5-FU resistance. Recent research [58], including our study, suggests that the combined usage of ferroptosis inducers and conventional therapies holds great promise in cancer treatment. **Second, a viable approach for 5FU-R CRC therapy is targeting DHODH-mediated pyrimidine synthesis, despite the cytosolic distribution of DHODH.** DHODH inhibitors are effective against cancer, either as monotherapy or in combination with anticancer agents [22], and are also utilized as anti-rheumatic [59] and broad-spectrum drugs [60] in clinical settings. Our study demonstrated that both *DHODH* knockdown and pharmacological inhibition effectively slowed CRC tumor growth and increased sensitivity to 5-FU. These findings concur with those of a previous report on the inhibition of DHODH with leflunomide resulting in increased gemcitabine sensitivity in gemcitabine-resistant pancreatic cancer [11]. The discovery of DHODH inhibitors may have significant implications for translational application in 5FU-R CRC therapy, particularly in light of the FDA approval and extensive clinical testing of teriflunomide. **Third, the vulnerability of mitochondria as a target in 5FU-R CRC has garnered our attention.** Recent evidence suggests that active mitochondria are essential for tumor growth [61], and numerous clinical trials are evaluating inhibiting mitochondrial function as a novel cancer therapeutic approach [62,63]. Our previous [19] and current studies have elucidated the irreversible and cumulative damage inflicted on 5FU-R CRC cell mitochondria, and its contribution to tumor progression and chemoresistance. Here, we attempted to partially rescue mitochondrial function through mitochondrial transplantation. Additionally, we induced oxidative stress to further impair mitochondrial function. Our findings suggest that mitochondria achieve a delicate equilibrium during the development of 5-FU resistance, but this has also exposed the targetable susceptibility of mitochondria.

A limitation of our study is the use of stable, 5-FU-resistant CRC cell lines as primary models for 5FU-R CRC tumor cells. To better replicate in vivo solid CRC tumors, we used a 3D spheroid culture, CDX models, and PDX models and conducted an observational cohort study with CRC patients who underwent preoperative fluorouracil analog-based chemotherapy. However, patients with 5-FU-resistant CRC frequently receive complex medical regimens that include pyrimidine analogs. Thus, currently, our findings should be considered preliminary and interpreted cautiously in clinical contexts.

5. Conclusions

Several molecular targeted strategies have been proposed to enhance 5-FU sensitivity or reverse 5-FU resistance in CRC; however, substantial progress remains elusive. This study provides promising novel insights into the impact of DHODH redistribution on ferroptosis susceptibility and pyrimidine biosynthesis augmentation in 5FU-R CRC. Therefore, targeting these vulnerabilities may facilitate overcoming 5-FU resistance in patients with CRC.

Ethics approval and consent to participate

All experiments involving experimental animals were approved by the Institutional Animal Care and Use Committee of Shandong Provincial Qianfoshan Hospital (2021 No.S603). All procedures complied with the relevant ethical standards for animal testing and research. The human studies followed the Declaration of Helsinki, were conducted with the informed consent of all the patients involved, and were approved by the Shandong Provincial Qianfoshan Hospital for research involving human subjects (2021 No.S1039).

Data statement

The clinicopathological data of the human subjects are summarized in Table S1. The primers used in the PCR are listed in Table S2. The gene list of the nucleotide metabolism PCR array plate is listed in Table S3. All data used and analyzed during the current study are available from the corresponding author upon reasonable request.

Funding

This work was supported by the National Natural Science Foundation of China [grant numbers 82303242, 82270914, 82270901]; and the Fundamental Research Funds for the Central Universities [grant numbers 2022JC024, 3332023028].

CRediT authorship contribution statement

Shuohui Dong: Formal analysis, Funding acquisition, Investigation, Methodology, Software, Visualization, Writing – original draft, Writing – review & editing. **Mingguang Zhang:** Data curation, Funding acquisition, Investigation, Methodology, Writing – review & editing. **Zhiqiang Cheng:** Conceptualization, Investigation, Methodology. **Xiang Zhang:** Conceptualization, Investigation, Methodology. **Weili Liang:** Funding acquisition, Investigation, Methodology. **Songhan Li:** Investigation, Methodology. **Linchuan Li:** Investigation, Methodology. **Qian Xu:** Investigation, Methodology. **Siyi Song:** Investigation, Methodology. **Zitian Liu:** Investigation, Methodology. **Guangwei Yang:** Investigation, Methodology. **Xiang Zhao:** Investigation, Methodology. **Ze Tao:** Investigation, Methodology. **Shuo Liang:** Formal analysis, Investigation, Methodology, Software, Visualization, Writing – original draft. **Kexin Wang:** Conceptualization, Funding acquisition, Project administration, Resources, Supervision, Visualization, Writing – review & editing. **Guangyong Zhang:** Conceptualization, Formal analysis, Project administration, Supervision, Writing – review & editing. **Sanyuan Hu:** Conceptualization, Funding acquisition, Project administration, Resources, Supervision, Validation, Writing – review & editing.

Declaration of competing interest

The authors declare that they have no known competing financial interests or personal relationships that could have appeared to influence the work reported in this paper.

Appendix A. Supplementary data

Supplementary data to this article can be found online at https://doi.org/10.1016/j.redox.2024.103207.

References

[1] F.A. Sinicrope, Increasing Incidence of early-onset colorectal cancer, N. Engl. J. Med. 386 (16) (2022) 1547–1558.
[2] C.G. Moertel, et al., Levamisole and fluorouracil for adjuvant therapy of resected colon carcinoma, N. Engl. J. Med. 322 (6) (1990) 352–358.
[3] S. Vodenkova, et al., 5-fluorouracil and other fluoropyrimidines in colorectal cancer: past, present and future, Pharmacol. Ther. 206 (2020) 107447.
[4] J. Ou, et al., ABHD5 blunts the sensitivity of colorectal cancer to fluorouracil via promoting autophagic uracil yield, Nat. Commun. 10 (1) (2019) 1078.
[5] C.L. Chen, et al., NANOG metabolically reprograms tumor-initiating stem-like cells through tumorigenic changes in oxidative phosphorylation and fatty acid metabolism, Cell Metabol. 23 (1) (2016) 206–219.
[6] M. Shahid, et al., S-palmitoylation as a functional regulator of proteins associated with cisplatin resistance in bladder cancer, Int. J. Biol. Sci. 16 (14) (2020) 2490–2505.
[7] S. Dong, et al., CD147 mediates 5-fluorouracil resistance in colorectal cancer by reprogramming glycolipid metabolism, Front. Oncol. 12 (2022) 813852.
[8] S. Solanki, et al., Dysregulated amino acid sensing drives colorectal cancer growth and metabolic reprogramming leading to chemoresistance, Gastroenterology 164 (3) (2023) 376–391 e13.
[9] C. Guo, et al., Therapeutic targeting of the mevalonate-geranylgeranyl diphosphate pathway with statins overcomes chemotherapy resistance in small cell lung cancer, Nat Cancer 3 (5) (2022) 614–628.
[10] S.J. Park, et al., Enhanced glutaminolysis drives hypoxia-induced chemoresistance in pancreatic cancer, Cancer Res. 83 (5) (2023) 735–752.
[11] S.K. Shukla, et al., MUC1 and HIF-1alpha signaling crosstalk induces anabolic glucose metabolism to impart gemcitabine resistance to pancreatic cancer, Cancer Cell 32 (1) (2017) 71–87 e7.
[12] S.J. Dixon, et al., Ferroptosis: an iron-dependent form of nonapoptotic cell death, Cell 149 (5) (2012) 1060–1072.
[13] V.S. Viswanathan, et al., Dependency of a therapy-resistant state of cancer cells on a lipid peroxidase pathway, Nature 547 (7664) (2017) 453–457.
[14] M.J. Hangauer, et al., Drug-tolerant persister cancer cells are vulnerable to GPX4 inhibition, Nature 551 (7679) (2017) 247–250.
[15] J. Tsoi, et al., Multi-stage differentiation defines melanoma subtypes with differential vulnerability to drug-induced iron-dependent oxidative stress, Cancer Cell 33 (5) (2018) 890–904 e5.
[16] M. Conrad, D.A. Pratt, The chemical basis of ferroptosis, Nat. Chem. Biol. 15 (12) (2019) 1137–1147.
[17] G. Lei, L. Zhuang, B. Gan, Targeting ferroptosis as a vulnerability in cancer, Nat. Rev. Cancer 22 (7) (2022) 381–396.
[18] C. Mao, et al., DHODH-mediated ferroptosis defence is a targetable vulnerability in cancer, Nature 593 (7860) (2021) 586–590.
[19] S. Dong, et al., ROS/PI3K/Akt and Wnt/beta-catenin signalings activate HIF-1alpha-induced metabolic reprogramming to impart 5-fluorouracil resistance in colorectal cancer, J. Exp. Clin. Cancer Res. 41 (1) (2022) 15.
[20] C. Yang, et al., De novo pyrimidine biosynthetic complexes support cancer cell proliferation and ferroptosis defence, Nat. Cell Biol. 25 (6) (2023) 836–847.
[21] D.R. Evans, H.I. Guy, Mammalian pyrimidine biosynthesis: fresh insights into an ancient pathway, J. Biol. Chem. 279 (32) (2004) 33035–33038.
[22] M. Bajzikova, et al., Reactivation of dihydroorotate dehydrogenase-driven pyrimidine biosynthesis restores tumor growth of respiration-deficient cancer cells, Cell Metabol. 29 (2) (2019) 399–416 e10.
[23] Y. Ma, et al., Synthetic lethal screening identifies DHODH as a target for MEN1-mutated tumor cells, Cell Res. 32 (6) (2022) 596–599.
[24] A. Martinez-Sabadell, et al., Protocol to generate a patient derived xenograft model of acquired resistance to immunotherapy in humanized mice, STAR Protoc 3 (4) (2022) 101712.
[25] S. Uchinomiya, et al., Fluorescence detection of metabolic activity of the fatty acid beta oxidation pathway in living cells, Chem. Commun. 56 (20) (2020) 3023–3026.
[26] E. Dierge, et al., Peroxidation of n-3 and n-6 polyunsaturated fatty acids in the acidic tumor environment leads to ferroptosis-mediated anticancer effects, Cell Metabol. 33 (8) (2021) 1701–1715 e5.
[27] J.J. Hu, et al., Fluorescent probe HKSOX-1 for imaging and detection of endogenous superoxide in live cells and in vivo, J. Am. Chem. Soc. 137 (21) (2015) 6837–6843.
[28] S. Ye, J.J. Hu, D. Yang, Tandem payne/dakin reaction: a new strategy for hydrogen peroxide detection and molecular imaging, Angew Chem. Int. Ed. Engl. 57 (32) (2018) 10173–10177.
[29] X. Bai, et al., HKOH-1: a highly sensitive and selective fluorescent probe for detecting endogenous hydroxyl radicals in living cells, Angew Chem. Int. Ed. Engl. 56 (42) (2017) 12873–12877.
[30] S. Wu, et al., Polymer functionalization of isolated mitochondria for cellular transplantation and metabolic phenotype alteration, Adv. Sci. 5 (3) (2018) 1700530.
[31] S. Liu, et al., Structures of human dihydroorotate dehydrogenase in complex with antiproliferative agents, Structure 8 (1) (2000) 25–33.
[32] J. Rawls, et al., Requirements for the mitochondrial import and localization of dihydroorotate dehydrogenase, Eur. J. Biochem. 267 (7) (2000) 2079–2087.
[33] Y.F. Lin, et al., A novel mitochondrial micropeptide MPM enhances mitochondrial respiratory activity and promotes myogenic differentiation, Cell Death Dis. 10 (7) (2019) 528.
[34] Y. Cao, Adipocyte and lipid metabolism in cancer drug resistance, J. Clin. Invest. 129 (8) (2019) 3006–3017.
[35] M. Bacci, et al., Fat and furious: lipid metabolism in antitumoral therapy response and resistance, Trends Cancer 7 (3) (2021) 198–213.
[36] J.A. Olzmann, P. Carvalho, Dynamics and functions of lipid droplets, Nat. Rev. Mol. Cell Biol. 20 (3) (2019) 137–155.
[37] T. Ueo, et al., White opaque substance represents an intracytoplasmic accumulation of lipid droplets: immunohistochemical and immunoelectron microscopic investigation of 26 cases, Dig. Endosc. 25 (2) (2013) 147–155.

[38] D.R. Green, The coming decade of cell death research: five riddles, Cell 177 (5) (2019) 1094–1107.
[39] S. Doll, et al., FSP1 is a glutathione-independent ferroptosis suppressor, Nature 575 (7784) (2019) 693–698.
[40] K. Bersuker, et al., The CoQ oxidoreductase FSP1 acts parallel to GPX4 to inhibit ferroptosis, Nature 575 (7784) (2019) 688–692.
[41] V.A.N. Kraft, et al., GTP cyclohydrolase 1/tetrahydrobiopterin counteract ferroptosis through lipid remodeling, ACS Cent. Sci. 6 (1) (2020) 41–53.
[42] P.H. Willems, et al., Redox homeostasis and mitochondrial dynamics, Cell Metabol. 22 (2) (2015) 207–218.
[43] J.T. Madak, et al., Revisiting the role of dihydroorotate dehydrogenase as a therapeutic target for cancer, Pharmacol. Ther. 195 (2019) 111–131.
[44] M. Fukushima, et al., Thymidylate synthase (TS) and ribonucleotide reductase (RNR) may be involved in acquired resistance to 5-fluorouracil (5-FU) in human cancer xenografts in vivo, Eur. J. Cancer 37 (13) (2001) 1681–1687.
[45] L. Gao, et al., Overcoming anti-cancer drug resistance via restoration of tumor suppressor gene function, Drug Resist. Updates 57 (2021) 100770.
[46] Y.G. Assaraf, et al., The multi-factorial nature of clinical multidrug resistance in cancer, Drug Resist. Updates 46 (2019) 100645.
[47] C. Cheng, et al., Glucose-mediated N-glycosylation of SCAP is essential for SREBP-1 activation and tumor growth, Cancer Cell 28 (5) (2015) 569–581.
[48] C. Cheng, et al., Lipid metabolism reprogramming and its potential targets in cancer, Cancer Commun. 38 (1) (2018) 27.
[49] N. Verma, et al., Synthetic lethal combination targeting BET uncovered intrinsic susceptibility of TNBC to ferroptosis, Sci. Adv. 6 (34) (2020).
[50] J.Y. Lee, et al., Polyunsaturated fatty acid biosynthesis pathway determines ferroptosis sensitivity in gastric cancer, Proc. Natl. Acad. Sci. U.S.A. 117 (51) (2020) 32433–32442.
[51] X. Jiang, B.R. Stockwell, M. Conrad, Ferroptosis: mechanisms, biology and role in disease, Nat. Rev. Mol. Cell Biol. 22 (4) (2021) 266–282.
[52] L.J. Yant, et al., The selenoprotein GPX4 is essential for mouse development and protects from radiation and oxidative damage insults, Free Radic. Biol. Med. 34 (4) (2003) 496–502.
[53] J. Du, et al., Identification of Frataxin as a regulator of ferroptosis, Redox Biol. 32 (2020) 101483.
[54] L. Jiang, et al., Ferroptosis as a p53-mediated activity during tumour suppression, Nature 520 (7545) (2015) 57–62.
[55] Y. Zhang, et al., BAP1 links metabolic regulation of ferroptosis to tumour suppression, Nat. Cell Biol. 20 (10) (2018) 1181–1192.
[56] P. Koppula, L. Zhuang, B. Gan, Cystine transporter SLC7A11/xCT in cancer: ferroptosis, nutrient dependency, and cancer therapy, Protein Cell 12 (8) (2021) 599–620.
[57] M. Conrad, et al., Regulation of lipid peroxidation and ferroptosis in diverse species, Genes Dev. 32 (9–10) (2018) 602–619.
[58] Y. Mou, et al., Ferroptosis, a new form of cell death: opportunities and challenges in cancer, J. Hematol. Oncol. 12 (1) (2019) 34.
[59] R.I. Fox, et al., Mechanism of action for leflunomide in rheumatoid arthritis, Clin. Immunol. 93 (3) (1999) 198–208.
[60] Y. Ma, et al., Medicinal chemistry strategies for discovering antivirals effective against drug-resistant viruses, Chem. Soc. Rev. 50 (7) (2021) 4514–4540.
[61] D.C. Wallace, Mitochondria and cancer, Nat. Rev. Cancer 12 (10) (2012) 685–698.
[62] C.R. Scafoglio, et al., Sodium-glucose transporter 2 is a diagnostic and therapeutic target for early-stage lung adenocarcinoma, Sci. Transl. Med. 10 (467) (2018).
[63] M. Benej, et al., Papaverine and its derivatives radiosensitize solid tumors by inhibiting mitochondrial metabolism, Proc. Natl. Acad. Sci. U.S.A. 115 (42) (2018) 10756–10761.